remote sensing

MDPI

Article

Multimodal and Multitemporal Drone Remote Sensing Approaches to Archaeological Prospection: The Case Study at the Medieval Castle of 't Huis ten Bosch, Weesp, The Netherlands

Mason Scholte [1,*] and Jitte Waagen [2]

[1] 4D Research Lab, University of Amsterdam, 1012 WX Amsterdam, The Netherlands
[2] 4D Research Lab/Amsterdam Center for Ancient Studies and Archaeology, University of Amsterdam, 1012 WX Amsterdam, The Netherlands; j.waagen@uva.nl
* Correspondence: l.m.scholte2@uva.nl

Abstract

This article evaluates the contribution of multi-temporal UAV remote sensing to archaeological prospection in a Dutch grassland context, using the moated castle site of 't Huis ten Bosch as a detailed case study. Six UAV campaigns, spanning more than four years and deploying thermal, multispectral, RGB and LiDAR sensors, are compared with magnetometry, electromagnetic induction, and coring data, and evaluated against seasonal and atmospheric conditions. The combined dataset corroborates and refines the subsurface record of the primary moat, secondary moat, and central tower and walls, demonstrating that no single prospection technique, applied in isolation, could have produced the same level of structural detail and interpretative confidence. A systematic comparison of anomaly visibility across campaigns shows that detectability varied considerably between campaigns, tracking soil properties, moisture history, vegetation phenology, and mowing regime, with the clearest results tending to coincide with transitional meteorological conditions instead of prolonged extremes, on the evidence of six campaigns. The study highlights both the promise and the site-specific constraints of UAV-based prospection, and identifies methodological limitations related to sensor availability, campaign density, and the use of regional meteorological data. It concludes by outlining some provisional best practices for UAV survey design and by arguing for stratified, multi-site implementations to develop a comparative empirical basis for optimising sensor deployment in archaeological prospection in the Netherlands and beyond.

Keywords: archaeological prospection; UAV; remote sensing; multi-modal; multi-temporal; thermal infrared; multispectral; lidar; castle; grassland

Check for updates

Academic Editor: Fulong Chen

Received: 13 August 2026
Revised: 20 October 2026
Accepted: 23 October 2026
Published: 8 November 2026

Copyright: © 2026 by the authors. Licensee MDPI, Basel, Switzerland. This article is an open access article distributed under the terms and conditions of the Creative Commons Attribution (CC BY) license.

1. Introduction

The Netherlands has a long and established tradition of archaeological prospection [1], formally organised around a protocolised workflow as set out in the national quality standard for archaeological research, the *Kwaliteitsnorm Nederlandse Archeologie* (KNA) [2]. This workflow is centred around the Archaeological Monument Care cycle (*Archeologische Monumentenzorg-cyclus;* AMZ-cycle), a sequence of consecutive steps concerned with the discovery, valuation, and safeguarding of archaeological remains, in which prospection provides the empirical foundation for all subsequent heritage management decisions.

In practice, prospection generally begins with a desk-based assessment, followed by a field survey in the form of fieldwalking or borehole survey (or both), and where

warranted, culminating in trial trenching [1]. This sequence, while effective for many contexts, tends to be applied uniformly in practice regardless of site-specific conditions, despite the choice of prospection technique directly shaping what can be detected and recorded in the subsurface [3]. This is further reinforced by the structural characteristics of the Dutch archaeological system, in which the competitive tendering of fieldwork contracts and the procedural rather than substantive nature of research specifications can discourage context-specific methodological adaptation [4].

For instance, geophysical methods, though capable of non-invasively characterising subsurface remains, are only applied sporadically within Dutch archaeological prospection [3,5], and where applied, their results have often not been used to guide subsequent investigation [5]. Remote sensing occupies an even more peripheral position: unlike geophysical survey, it lacks even formal recognition within the KNA as a prospection method [6]. This is despite ongoing developments in the field, where low-altitude remote sensing in particular has increasingly demonstrated its potential for archaeological prospection.

Already for over a decade, the proliferation of affordable yet powerful unmanned aerial vehicles (UAVs, also known as 'drones') and the concurrent miniaturisation and improvement of sensor technologies have significantly expanded the potential for low-altitude aerial remote sensing in archaeological prospection [7,8]. Sensor modalities including multispectral cameras, thermal infrared sensors, and LiDAR can now be integrated into small drone systems and deployed with a high degree of operational flexibility. Beyond the practical advantages of cost and accessibility, low-altitude acquisition also offers inherent physical benefits: reduced atmospheric path length limits the amount of spectral signal lost through attenuation, especially important for thermal imaging [9], whilst the proximity to the surface simultaneously yields extremely high spatial resolutions relative to other remote sensing platforms, like satellites.

In contrast to the Netherlands, remote sensing, specifically using UAVs, has become considerably better integrated into archaeological heritage management elsewhere. In the United Kingdom, systematic aerial survey programmes dating back to the early twentieth century have established a long tradition of remote sensing in archaeological practice [10], with national heritage management bodies such as Historic Environment Scotland actively integrating drone remote sensing in their prospection workflows [11]. Comparable developments are evident in Scandinavia, where UAV-borne LiDAR in particular has gained traction in prospection practice for forested landscapes [12].

Where UAVs are applied in Dutch archaeological practice, their use has remained largely confined to RGB photogrammetry for the documentation of excavations [13]. Sensor modalities beyond the visible spectrum, like those in the near-infrared or thermal longwave infrared, remain virtually absent from commercial archaeological practice, and the deployment of UAVs as an active prospection tool is the exception rather than the rule. Although successful Dutch examples of remote sensing-based prospection do exist [13–16], these have not translated into structural integration within the AMZ cycle.

The limited uptake of remote sensing within Dutch archaeological practice is, however, not simply a matter of institutional inertia. A more fundamental obstacle lies in the variable outcomes of sensor-based archaeological prospection [6], stemming less from the applied techniques themselves than from a poor understanding of the conditions under which a given sensor reliably produces interpretable archaeological signals. The detectability of archaeological features is dependent on an interconnected set of variables, encompassing the nature and depth of subsurface remains, soil composition and moisture conditions, land use and vegetation state, sensor characteristics and acquisition parameters, and prevailing meteorological conditions at the time of capture [17–20]. This makes it difficult for practitioners to predict when and whether deployment will yield meaningful prospection

results [6]. Different sensor modalities also respond to distinct physical properties of the soil and vegetation and therefore capture different aspects of the subsurface archaeological record. Understanding the relative effectiveness of individual sensor types, and what can be gained by deploying them in combination, consequently, forms an integral part of this broader knowledge gap.

Addressing this knowledge gap requires systematic investigation at sites where subsurface conditions have been characterised by means of other prospection techniques such as geophysical prospection or coring. This allows sensor-derived anomalies, defined in this paper as localised relative contrasts or deviations in sensor readings (e.g., in elevation, reflectance, temperature, or tone) that are not immediately attributable to a known natural process or documented modern land use, to be evaluated against independent subsurface evidence rather than interpreted in isolation. Such studies are accumulating internationally, with multi-sensor UAV campaigns reported across a range of environmental and pedological contexts [9,21–27]. Within the Netherlands, first steps in this direction are similarly being taken [9,13,15,16].

The present paper addresses this need by presenting the results of a multi-temporal, multi-modal UAV prospection campaign conducted at the medieval castle site of 't Huis ten Bosch near Weesp, Noord-Holland, The Netherlands. Across six acquisition campaigns conducted between 2022 and 2026, spanning a range of seasonal and meteorological conditions, drone-borne LiDAR, multispectral, RGB, and thermal sensors were deployed to survey the archaeological landscape, with the aim of examining the conditions under which each sensor modality produces interpretable representations of archaeological features. Imagery from each campaign was analysed to identify spectral, thermal, and structural anomalies indicative of subsurface archaeological remains, and their detectability was examined in relation to sensor type, season, meteorological conditions, and land management practices at the site, to establish how these factors, in combination, affect the visibility of archaeological anomalies in low-altitude remote sensing data at this site.

Three questions are addressed in particular: (i) which sensor modalities resolve which of the subsurface features at the site; (ii) how the detectability of those features varies between campaigns in relation to season, antecedent meteorological conditions, vegetation state and land management; and (iii) what the multi-temporal series implies for the timing and composition of UAV prospection at grassland sites of this kind. These questions are addressed in Sections 4.1, 4.2 and 5, respectively. Detectability is treated here as a documented interpretative judgement rather than a measured quantity. An anomaly is recorded as detected in a given dataset when it meets the definition given above on visual inspection of that dataset, and each record carries a confidence score for the anomaly and for its archaeological interpretation, together with the observational conditions under which it was assessed (Section 2.4; Table A1). This gives a consistent and auditable basis for comparison across campaigns and sensors, but it remains an ordinal assessment.

't Huis ten Bosch (52.2922°N, 5.0763°E) is a medieval castle whose remains lie buried beneath pastureland on the eastern bank of the river Vecht, near the modern town of Weesp in Noord-Holland (Figure 1). First referenced in a historical source in 1244, the castle occupied a strategically significant position in the borderlands between the County of Holland and the Prince-Bishopric of Utrecht, and its history was marked by repeated destruction and rebuilding before its final demolition following the Dutch Republic's *Rampjaar* of 1672. Above-ground masonry was removed after its final demolition, leaving subsurface structural remains whose full extent and preservation remain only partly understood. Subtle surface traces, including relief differences visible in raking light and vegetation discolorations reported during dry summers, suggest that buried remains continue to influence surface conditions, making the site an apt test case for multi-sensor UAV prospection. A

targeted geophysical survey and coring campaign, both conducted in early 2022, established a baseline subsurface record against which the interpreted archaeological anomalies from the remote sensing results presented in this paper are assessed.

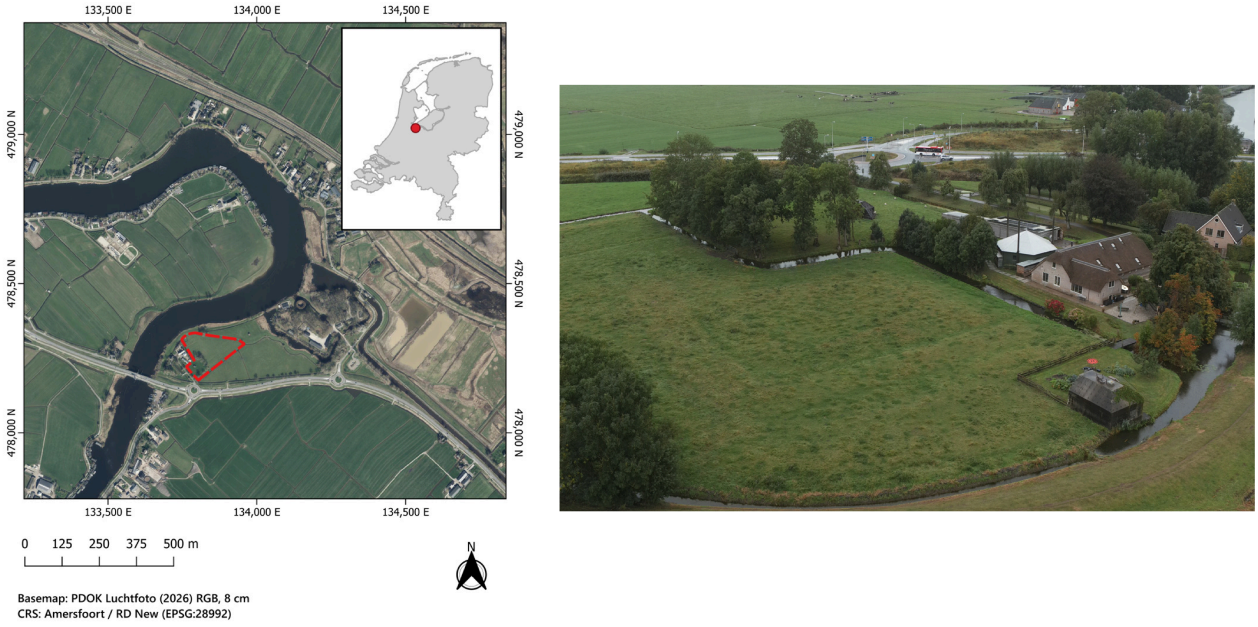


Figure 1. (**left**) Location of the case study site; (**right**) Oblique aerial overview of the pastureland containing 't Huis ten Bosch, viewed from the north during the September 2025 UAV campaign.

The initial investigations at the site 't Huis ten Bosch were commissioned by the Municipality of Amsterdam and initiated by Ranjith Jayasena. They comprised geophysical prospection conducted by Ferry van den Oever and a coring programme undertaken by the commercial firm Hollandia Archeologen. Collectively, these activities yielded a first interpretative assessment of the site, to which Nancy de Jong-Lambregts also contributed [28]. In addition, the location constituted one of the case studies serving as a designated test site within the ARCfieldLAB project, which aims to promote the implementation of sensor technologies in Dutch field archaeology [6].

2. Materials and Methods

2.1. Case Study Site

2.1.1. Historical Context

The castle of Huis ten Bosch has had a turbulent history, both in its medieval lifetime and in the centuries following its final destruction. The site lies in the historical borderlands between the County of Holland and the Prince-Bishopric of Utrecht (Het Sticht), on the eastern bank of the river Vecht near the modern-day town of Weesp. In the 13th century, the Vecht formed a strategically significant frontier, and the territorial rivalry between the Bishop of Utrecht and the Counts of Holland over control of this waterway is reflected in the castles built along its course [28,29].

It was against this backdrop that the Van Amstel family came into the possession of the estate: in 1226, Gijsbrecht II acquired jurisdiction over Weesp, Muiden, Diemen, and the surrounding Uitermeer area, subsequently granting the "ten Bosch" property to his brother Egbert. A castle is unlikely to have existed here at this stage, with the construction likely occurring sometime thereafter, under either Gijsbrecht II or Egbert. The first documented reference to the castle dates to 1244, when Egbert's son is recorded under the name "van den Bosch" [30]. A 1439 feudal record describes the property as comprising a castle with

a bailey and an orchard within the outer moat, along with waterworks (sluices) located elsewhere on the estate [28,29].

The castle's history over the centuries following its construction was marked by repeated destruction and rebuilding [28–30]. It was captured in 1374 by an episcopal fleet during a conflict between Utrecht and Holland, alongside Muiden, Weesp, Loosdrecht, and Kronenburg, besieged and destroyed again in 1408 by the Count of Holland, Willem IV, and once more in 1426 by Duke Philip of Burgundy. A further attack in 1514, this time by Frisian rebels together with mercenaries from the Duchy of Guelders, left the castle ruined once again, and as late as 1572 it had still not been restored. Its final destruction came in the *Rampjaar* ("Disaster Year") of 1672, when the Dutch Republic was invaded simultaneously by France, England, and the German Prince-Bishoprics of Münster and Cologne. Although the invading French forces left the already-ruined castle largely intact, it was ultimately never rebuilt and was torn down the following year [28]. As was common practice for such demolitions, the above-ground masonry and upper foundations were likely cleaned of mortar and sold for reuse, while the deepest and most solid foundation work (the so-called *gegoten werk* or 'poured structures') was left in situ, though even these remnants were reportedly dug out and carted away around 1925 [30].

Surviving depictions of Huis ten Bosch, such as the drawing from the Atlas Schoenmaker (Figure 2, left), all postdate the castle's final destruction. As a result, it is uncertain whether the elements they appear to show are accurate reflections of the castle's actual layout. Clues pointing to the extent of the former castle grounds also survive in historical maps: the 1832 cadastral map, for instance, clearly shows a moat near the site of the (later-built) farmhouse (Figure 2, right), and the name Huis ten Bosch itself persisted on these maps as the name of that farm. Shortly before the start of the Second World War, a series of casemate defences were erected along the river to bolster the defensive line around Amsterdam, and it appears that the former moat was filled in around this same time [28]. The site is currently used as pastureland for sheep, but remains of the castle still mark the terrain. In raking sunlight, subtle relief differences trace the moat and square outline of a tower, and in particularly dry summers these features have reportedly become visible as discolorations in the grass. The grassland cover is predominantly a *Lolium* species, most likely perennial ryegrass (*Lolium perenne*) given its prevalence in Dutch pastureland. Some clover was also visible in the field, though no formal floristic survey was carried out to establish the full species composition of the sward.

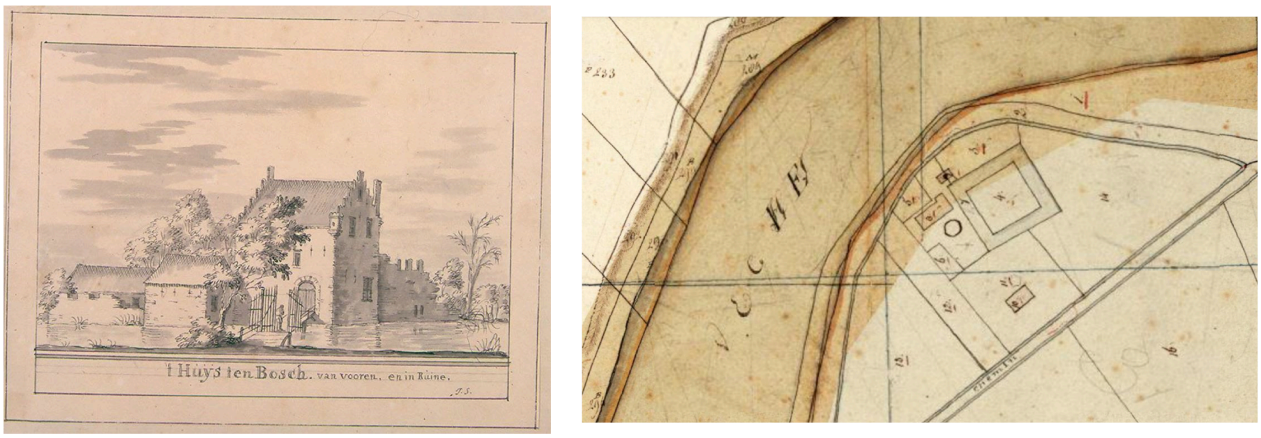


Figure 2. (**left**) 18th-century drawing of 't Huys ten Bosch, artist unknown. The inscription on the drawing reads "'t Huys ten Bosch, van vooren, en in Ruïne" ("'t Huys ten Bosch, from the front, and in ruins"). Collection Atlas Schoemaker, Noord-Hollands Archief; (**right**) the site's location on the 1832 national cadastral plan (Kadastraal Minuutplan), on which the square moat is clearly visible.

2.1.2. Concurrent Non-Invasive Research

In early 2022, a geophysical prospection survey and a hand augering campaign were carried out in parallel with the first UAV acquisition campaign presented in this study. These followed the incorporation of the former municipality of Weesp into Amsterdam in 2022, which brought the site's archaeological management under the responsibility of the Amsterdam city archaeologists. Given the absence of any immediate development threat, these investigations were deliberately designed as non-destructive, with the explicit aim of establishing what could be learned about the buried remains of 't Huis ten Bosch without resorting to trial trenching.

The geophysical survey was carried out by Saricon B.V. between 24 and 26 January 2022 [31], combining magnetometry (four Vallon 1302D gradiometer sensors (VALLON GmbH, Enningen, Germany) mounted on a non-magnetic cart) with electromagnetic induction (a CMD mini-explorer (GF Instruments s.r.o., Brno, Czechia), recording both electrical conductivity and magnetic susceptibility) (for more in-depth information on the methodology, see [31]). Both techniques traced a rectangular pattern of high-contrast anomalies in the northwestern part of the surveyed area (Figure 3, centre and right), interpreted as the foundation of a tower measuring approximately 12 m by 12 m with walls between 2 m and 3 m thick, surrounded by a zone of dense, iron-rich rubble attributed to the demolished castle. An anomaly of lower conductivity and weaker magnetic contrast around this rubble zone was interpreted as the primary moat, and subtle differences within the magnetometry data allowed this moat to be traced around the structure. Parts of this moat showed magnetic contrasts, pointing to the possible use of bricks or other building material to fill the moat. A shallow northwest–southeast depression in the topography of the site roughly 40 m further to the northeast suggested a possible second, more distant moat. Although this feature also appeared as an anomaly in the geophysical data, its existence could not be confirmed with certainty on that basis alone.

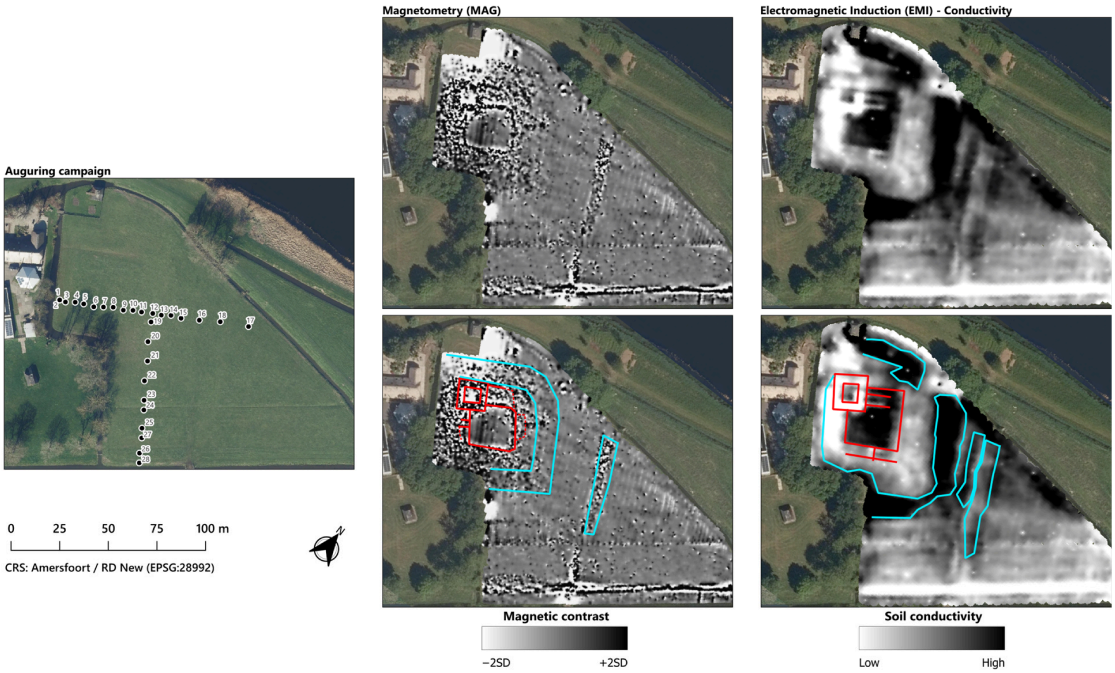


Figure 3. Overview of the 2022 non-invasive prospection results at 't Huis ten Bosch. (**left**) Locations of the hand-augered boreholes by Hollandia Archeologen; (**centre**) results of the magnetometry survey by Saricon B.V.; (**right**) results of the electromagnetic induction survey by Saricon B.V. In (**lower centre**) and (**lower right**), red outlines mark the interpreted structural features, and cyan outlines mark interpreted terrain-related features.

This was followed on 28 February 2022 by a coring survey carried out by Hollandia Archeologen [32]. Twenty-nine hand-augered boreholes were placed along two perpendicular transects across the presumed castle site and its surrounding moats (Figure 3, left), to a maximum depth of 2.5 m below surface, revealing a subsoil that consisted predominantly of river clay. The corings provided insights into the stratigraphy of the site and confirmed the presence of a moat circling the foundation of the castle, filled with clay and demolition rubble overlying a thin peat layer interpreted as the original moat bottom. Foundation material or heavy brick rubble was struck at a shallow depth of around 0.35 m below surface within the area corresponding to the tower as defined by the geophysical survey. A single borehole (core 18) placed at the presumed course of the secondary moat did strike a ditch or moat fill of clay and rubble. Its exact relation to the castle cannot be determined with certainty on this basis alone, but, as with the geophysical survey, the location and composition of the fill make a connection plausible.

These surveys together provide the independent subsurface evidence against which the UAV results are compared in this paper. Each samples the subsurface in a different way: the geophysics records contrasts in magnetic and conductivity response across the whole field, while the twenty-nine boreholes observe material directly at points along two transects. Section 4.1 accordingly reads the three records against one another, with none of them serving as a "complete" ground truth against which the others could be scored.

2.2. Multi-Temporal and Multi-Modal UAS-Surveys

2.2.1. Overview of the Campaigns

A total of six UAV acquisition campaigns were conducted at the site of 't Huis ten Bosch between February 2022 and April 2026, with three separate campaigns flown within 2022 alone. The datasets of 9 February, 2 June, and 9 September were captured that year, with single campaigns conducted on 15 August 2024, 9 September 2025, and 30 April 2026. The timing of individual campaigns was roughly planned but also depended partly on practical possibilities. The resulting dataset spans winter, spring, and summer/early autumn conditions, allowing seasonal variation in feature detectability to be explored across the multi-year series. Across all six campaigns, a consistent survey area covering the pastureland containing the main castle grounds was maintained, with coverage extended to the adjacent fields when time permitted. Alongside this temporal spread, the campaigns combined multiple sensors, deploying multispectral, thermal, LiDAR, and RGB sensors in combination. Not every campaign included all four technologies, as, for example, the LiDAR sensor was only acquired after the first campaigns, and the specific weather conditions did not allow each sensor to be used every time. Thermal imagery, for instance, could not be captured during rainfall, as rainfall reduces thermal contrast to the point where the resulting imagery is too uniform to support photogrammetric reconstruction. Table 1 summarises the sensor deployment and data acquisition parameters in each campaign. Full flight parameters for all campaigns are provided in Supplementary Materials Table S1.

Table 1. Sensor deployment and acquisition parameters across the six UAV campaigns at 't Huis ten Bosch.

Campaign	Sensor	Platform	Time	Altitude AGL	Overlap % (Side/Front)	Images	Ground Control	Data Resolution
9 February 2022	RGB—Zenmuse X5S	DJI M210	12:00	45 m	70/80	492	6 GCPs, dGPS (RMS 0.009 m)	1.0 cm
	Multispectral—RedEdge-MX	DJI M210	11:20	45 m	70/80	4257	6 GCPs, dGPS (RMS 0.0345 m)	3.4 cm
	Thermal—not acquired; rainfall during the campaign LiDAR—not acquired; sensor not yet available							

Table 1. *Cont*.

Campaign	Sensor	Platform	Time	Altitude AGL	Overlap % (Side/Front)	Images	Ground Control	Data Resolution
2 June 2022	RGB—not acquired; sensor malfunction							
	Multispectral—RedEdge-MX	DJI M210	13:15	50 m	70/80	2395	6 GCPs, dGPS (RMS 0.0681 m)	3.5 cm
	Thermal—Zenmuse XT2	DJI M210	22:00	100 m	75/85	67	8 GCPs, dGPS (RMS 0.944 m)	22.9 cm
	LiDAR—not acquired; sensor not yet available							
9 September 2022	RGB—Zenmuse X5S	DJI M210	11:30	50 m	70/80	346	6 GCPs, dGPS (RMS 0.011 m)	1.6 cm
	Multispectral—RedEdge-MX	DJI M300 RTK	13:30	70 m	70/80	1495	Network RTK, D-RTK 2 base	7.2 cm
	Thermal—Zenmuse XT2	DJI M210	20:00	120 m	75/85	301	6 GCPs, dGPS (RMS 0.301 m)	16.6 cm
	LiDAR—Zenmuse L1	DJI M300 RTK	12:30	50 m	—	—	Network RTK, D-RTK 2 base	1.5 cm (DTM)
15 August 2024	RGB—Zenmuse P1	DJI M300 RTK	11:30	100 m	70/80	384	Network RTK, 06GPS	1.0 cm
	Multispectral—RedEdge-MX	DJI M300 RTK	12:50	50 m	70/80	5495	Network RTK, 06GPS	3.5 cm
	Thermal—Zenmuse XT2	DJI M300 RTK	14:15	60 m	75/85	772	Network RTK, 06GPS	7.7 cm
	LiDAR—Zenmuse L1	DJI M300 RTK	12:15	50 m	—	—	Network RTK, 06GPS	1.5 cm (DTM)
9 September 2025	RGB—Zenmuse P1	DJI M350 RTK	14:40	120 m	70/80	67	Network RTK, 06GPS	1.5 cm
	Multispectral—RedEdge-P	DJI M350 RTK	14:15	50 m	75/85	1584	Network RTK, 06GPS	6.4 cm
	Thermal—not acquired; rainfall during the campaign							
	LiDAR—Zenmuse L2	DJI M350 RTK	14:30	60 m	—	—	Network RTK, 06GPS	1.5 cm (DTM)
30 April 2026	RGB—Zenmuse P1	DJI M350 RTK	13:35	120 m	70/80	183	Network RTK, 06GPS	1.5 cm
	Multispectral—RedEdge-P	DJI M350 RTK	12:30	70 m	75/85	5136	Network RTK, 06GPS	7.2 cm
	Thermal—Zenmuse H30T	DJI M350 RTK	21:45	80 m	75/85	803	Network RTK, 06GPS	4.0 cm
	LiDAR—Zenmuse L2	DJI M350 RTK	13:00	50 m	—	—	Network RTK, 06GPS	1.5 cm (DTM)

2.2.2. Hardware Evolution and Geolocation

Over the course of the campaigns, both the UAV platform and sensor payloads were progressively upgraded as newer equipment became part of the available 4DRL arsenal. This progression is a natural feature of a multi-year study, with each new generation of hardware offering gains in spatial resolution and radiometric precision over its predecessor (see Supplementary Materials Table S1 for details on the sensor specifications). Section 4.3 considers what this implies for the comparison between campaigns.

The upgrading of the platform did affect how flights were georeferenced. Earlier campaigns, flown using the M210 (DJI, Shenzen, China),, relied on six ground control points (GCPs) spread across the study area. These were measured using a GeoMax Zenith15 GNSS receiver (GeoMax, Widnau, Switzerland) connected to the Dutch 06-GPS NTRIP network. From the September 2022 campaign onward, GCPs were replaced by the DJI M300's (DJI, Shenzen, China), onboard high-quality real-time kinematic (RTK) positioning, similarly connected to the 06-GPS network. One exception remained: the thermal acquisition within that same campaign was still flown on the M210 and therefore continued to rely on GCP-based georeferencing. All subsequent campaigns used RTK positioning exclusively.

2.2.3. Sensor-Specific Acquisition Protocols

During every visit to 't Huis ten Bosch, a multispectral sensor was used. Multispectral remote sensing is widely used in archaeological prospection to detect subtle variations in the reflection, absorption, or scattering of visible and near-infrared light. These variations arise from differences in the material properties of vegetation and soil, which can in turn reflect the growth or stress responses of crops and grasses growing above buried archaeological remains [18,33]. In the surveys, the multispectral acquisitions were timed within two hours of solar noon to maximise the amount of incoming solar radiation. The earlier surveys made use of the MicaSense RedEdge-MX (MicaSense, Seattle, WA, USA) [34], which provided spectral data across five bands: blue, green, red, red-edge, and near-infrared. The RedEdge-P (MicaSense, Seattle, WA, USA), used in the later campaigns [35], added an additional panchromatic band (Table 2). This band was not used in processing, so that all six campaigns are compared across the same five spectral bands. To subsequently radiometrically calibrate these collected data, a MicaSense calibrated reflectance panel was photographed immediately before and after each flight. In addition, to compensate where possible for the effects of any mid-survey variations in light conditions, a Downwelling Light Sensor (DLS) (MicaSense, Seattle, WA, USA) was mounted to the drone and connected to the multispectral sensor to record incident irradiance during the flights.

Table 2. Spectral band specifications of the multispectral sensors used.

Sensor	Spectral Band	Center Wavelength (nm)	Bandwidth (nm)
MicaSense RedEdge-MX	Blue	475	32
	Green	560	27
	Red	668	14
	Red Edge	717	12
	Near-Infrared (NIR)	842	57
MicaSense RedEdge-P	Blue	475	32
	Green	560	27
	Panchromatic	634	463
	Red	668	14
	Red Edge	717	12
	Near-Infrared (NIR)	842	57

In several of the surveys, a thermal imaging sensor was additionally deployed: a Zenmuse XT2 sensor (DJI, Shenzen, China) was used in earlier campaigns [36], replaced by a Zenmuse H30T (DJI, Shenzen, China) in the final campaign [37]. Thermal remote sensing in archaeological prospection relies on the fact that different materials heat up and cool down at different rates, a behaviour determined by each material's conductivity, heat capacity, and thermal inertia. As a result, subsurface remains and their surrounding soil retain and release heat differently over the course of a day, producing measurable temperature contrasts at the surface [9,20,38,39]. Thermal sensors measure long-wave radiation emitted by the surface itself, as determined by its temperature and emissivity [39]. During daylight, solar heating dominates the surface energy balance. Surface temperatures then depend largely on how much radiation each part of the field absorbs, governed by factors such as albedo, slope and aspect, and shading, which readily masks the subtler contrasts arising from the thermal properties of buried remains. Once direct solar input ceases after dusk, this daytime heating gives way to a steadier, more uniform cooling as the surface settles towards equilibrium with the cooling air. During this phase, the differing thermal inertia of buried material and the surrounding soil increasingly governs how quickly each releases its stored heat. This preference is not absolute where vegetation is present. Canopy temperature is

also regulated by evapotranspiration, so differences in root-zone moisture above buried features can register indirectly during daylight, and Ciccone [40] reports mid-morning and mid-afternoon acquisitions outperforming both pre-dawn and post-sunset flights over densely cropped fields on this basis. In frequently mown pasture, however, canopy density and transpiration are considerably lower than in a maturing cereal crop. Acquisitions at Weesp were therefore made in the evening, following the pattern reported for comparable mown grassland [41] and timed to capture this post-sunset cooling window, well before the dew point is typically reached later in the night. Rising humidity and dew point onset have been suggested to dampen thermal contrasts, though their relative influence compared to ongoing soil cooling remains unclear [9,20].

LiDAR data were collected starting from September 2022 onwards to generate high-resolution elevation models capable of identifying microtopographic anomalies associated with buried remains. A Zenmuse L1 (DJI, Shenzen, China) was used until 2025, after which a Zenmuse L2 (DJI, Shenzen, China) was used. The L2 represents an upgrade over the L1, offering more returns (five for the L2 over the three of the L1) and better vertical and horizontal accuracy (4 cm and 5 cm, respectively, compared to 5 cm and 10 cm for the L1) [42,43]. As the L2 is a direct successor to the L1, offering mainly improvements in point density and accuracy, this change is not expected to have affected comparability across the dataset, particularly given the low vegetation density of the research area. Unlike the RGB, multispectral, and thermal acquisitions, LiDAR flights were not constrained by specific illumination or timing requirements and were thus flown whenever convenient within each campaign. From the 2025 survey onward, an additional flightline was flown perpendicular to the standard back-and-forth pattern to aid alignment of individual flight strips during post-processing.

RGB imagery, captured with a Zenmuse X5S (DJI, Shenzen, China) [44] in earlier campaigns and a Zenmuse P1 (DJI, Shenzen, China) [45] in later ones, served as a visual reference to aid in the interpretation of anomalies detected using the other sensor modalities. Where possible, the RGB images were captured in favourable illumination conditions, with flights avoided when harsh shadows fell across areas of interest, broadly consistent with the timing applied to multispectral acquisition.

2.3. Data Processing

For an overview of the specific parameters used in the following sections concerning data processing, see Supplementary Materials Table S2.

2.3.1. Multispectral Data

For each campaign, the multispectral imagery and accompanying pre- and post-flight calibration images were loaded into Agisoft Metashape Professional 2.3.1. The imagery was then radiometrically calibrated using the panel images and the DLS data stored in each image's EXIF metadata, while making sure that the calibration panel masks covered only the panel itself. Following the standard photogrammetric workflow, a multi-band orthomosaic containing all multispectral bands expressed in reflectance values, rather than raw digital numbers, was generated for each campaign. The resulting multi-band orthomosaics were imported into QGIS 3.44.1 [46], where a series of vegetation indices were calculated for each campaign (Table 3).

Table 3. Overview of the calculated vegetation indices in this study.

Index	Formula	Reference
NDVI (Normalized Difference Vegetation Index)	$\frac{(NIR-Red)}{(NIR+Red)}$	Rouse et al. [47]
NDRE (Normalized Difference Red Edge Index)	$\frac{(NIR-RedEdge)}{(NIR+RedEdge)}$	Barnes et al. [48]
GNDVI (Green Normalized Difference Vegetation Index)	$\frac{(NIR-Green)}{(NIR+Green)}$	Gitelson et al. [49]
MSAVI2 (Second Modified Soil Adjusted Vegetation Index)	$\frac{2*NIR+1-\sqrt{(2*NIR+1)^2-8(NIR-Red)}}{2}$	Qi et al. [50]
EVI (Enhanced Vegetation Index)	$2.5 * \frac{NIR-Red}{NIR+6*Red-7.5*Blue+1}$	Huete et al. [51]

2.3.2. Thermal Data

Raw thermal imagery from the XT2 sensor is collected as R.JPG files, a proprietary encoding that embeds the radiometric data and thermal emission values within the JPEG file format. Before being used to generate a thermal orthomosaic, these images were processed in FLIR Thermal Studio Pro 2.0, which extracts the embedded thermal data and, by applying emissivity and atmospheric correction parameters, converts the raw imagery into a set of 14-bit radiometric TIFFs. Data collected using the H30T is stored in a similar yet distinct proprietary format, T.JPG, which FLIR Studio Pro cannot process. Moreover, DJI's own DJI Thermal Analysis Tool 3 software does not provide radiometric calibration capability [52]. The files were thus instead calibrated using WebODM's ThermalTools 1.2.0 [53], which applies a comparable emissivity and atmospheric correction to convert the T.JPGs into radiometric TIFF files.

The resulting radiometric imagery from both sensors was subsequently processed in Pix4Dmapper 4.10.1 following a standard photogrammetric workflow to generate a thermal orthomosaic for each campaign, which was subsequently loaded into QGIS.

As the deployed thermal sensors are uncooled, they are prone to a gradual, macro-scale temperature drift as they warm up over the course of a survey, unrelated to the actual thermal properties of the ground.

Although Paulsen et al. [54] recently showed a custom setup to mitigate this effect successfully, in this study the sensor was used with no further enhancements. The drift was instead corrected using the post-processing method described by Hill et al. [24]. This involved generating a low-pass filtered version of each thermal orthomosaic and subtracting it from the original, isolating local thermal contrast while removing the broader drift trend. In practice, this was achieved in QGIS by applying a 5 m low-pass filter using SAGA 9.12.4's Resampling Filter tool [55], with the scale factor parameter set to achieve a window scaled to the resolution of each individual thermal orthomosaic. A mean filter with a radius of 5 m (a 61 by 61 pixel kernel at the 16.6 cm resolution of the September 2022 mosaic) gave the best approximation of the drift trend while preserving local thermal contrast in the September 2022 capture. The same ground distance was applied to the other thermal maps, with the kernel size scaled to each mosaic's resolution (Figure 4).

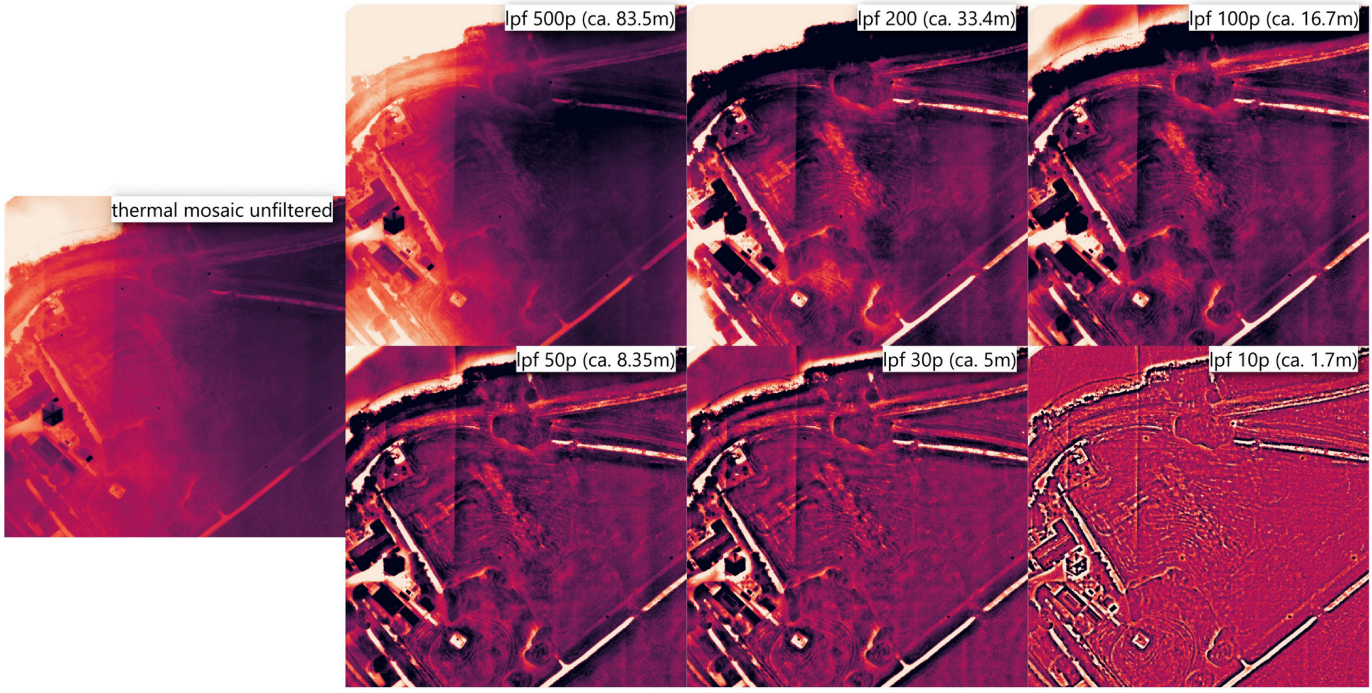


Figure 4. Filter-size sensitivity analysis for the thermal drift correction, shown for the September 2022 thermal mosaic. The leftmost panel shows the unfiltered thermal mosaic. The other panels show the mosaic with the low-pass filter applied, for mean filter radii of 500, 200, 100, 50, 30 and 10 pixels.

2.3.3. LiDAR Data

The points acquired by the DJI L1 and L2 LiDAR sensors are stored in the proprietary LDR format. As a first step, these files were processed in DJI Terra 5.3.0 [56] to produce a single LAS point cloud. After this, the alignment of the individual swaths was improved. Even with the highly accurate RTK receiver in the M300 drone and the inertial measurement unit (IMU) embedded within the L1 and L2 sensors, adjacent flight strips rarely align perfectly, as small errors in IMU-recorded attitude and position, together with positioning inaccuracies, accumulate over a flight and produce discrepancies between overlapping swaths. These misalignments lead to a pronounced striping artifact on the final digital elevation models (DEMs). To correct for this, the collected LiDAR point clouds were processed using BayesMap StripAlign 2.28 [57], which registers overlapping swaths and corrects both relative and absolute geometric errors using a time-dependent approach capable of accounting for IMU drift and vibrations of the platform throughout the flight.

Next, the corrected flight strips were tiled using *lastile64* tool from the LAStools 2.0.5 software package [58] to ensure the following processing steps would not result in memory-related errors.

To pick out only the ground points needed to construct a digital terrain model (DTM), the point cloud tiles were processed in R 4.6.1 using the lidR package [59,60]. Ground points were classified using a Progressive TIN Densification (PTD) algorithm, which iteratively builds a triangulated surface from likely ground points while excluding vegetation and other non-ground returns (for a more in-depth overview of the method, see [61]). The resulting ground point clouds were then rasterised using TIN interpolation and merged into a single DTM covering the full survey area for each campaign, which was then loaded into the QGIS project.

2.3.4. RGB Data

The RGB imagery from each campaign was processed in either Pix4Dmapper 4.10.1 [62] or Agisoft Metashape Professional 2.3.1 [63] following a standard photogrammetric processing workflow, comprising image alignment, dense point cloud generation, and lastly, the creation of the orthomosaic and its subsequent export. For the earlier campaigns in which no LiDAR data were acquired, the digital surface model (DSM) derived from the RGB point cloud served as the height reference for the analysis. These data models were all loaded into QGIS for further remote sensing analysis of the site.

2.4. Remote Sensing Anomaly Analysis

Following processing and visualisation, the four sensor datasets from each campaign were loaded as layers in QGIS, onto which candidate anomalies were mapped directly. Anomaly identification and interpretation followed a two-step procedure. The first step consisted of visual inspection of each processed sensor output to identify topographic irregularities, spectral contrasts, or thermal marks that stood out from their surroundings. Interpretation relied on relative contrast within each output rather than on absolute sensor values. During inspection, each raster was accordingly examined under a range of contrast enhancements, including histogram stretches applied both across the full survey area and to smaller sub-areas, so that variation could be assessed at different scales without reference to absolute values. Anomalies were digitised as line vectors following the extent of the observed contrast. A single feature may therefore be represented by more than one record, as when both edges of a ditch or moat were traced separately. The visibility score recorded for each anomaly refers to the local contrast that led to its identification, and not to how completely a feature is represented in a given dataset. In the second step, anomalies that could not be readily explained by natural processes or by modern land use were assessed and interpreted in terms of their potential archaeological origin. This interpretation drew on the landscape history of ‘t Huis ten Bosch, typological comparison with known medieval castle features, and comparison with the subsurface record established by the coring campaign and geophysical prospection, to arrive at a probable archaeological explanation for each anomaly. These two steps serve different purposes and are kept separate in the analysis that follows. The first establishes whether something is detectable in a given dataset, using a criterion internal to the image: a feature either stands out from its surroundings or it does not. Reference material from the geophysical survey and coring campaign enters only at the second step, where it informs what an anomaly might represent. The comparison of detectability between campaigns in Section 4.2 therefore rests on the first step alone, while Section 4.1 presents the archaeological interpretation, which draws on all available evidence as it should.

Each mapped anomaly was recorded in a standardised metadata table (Table A1) to ensure consistency across the six campaigns and four sensor types (following the table of [64], adapted from the original scheme by Lozić and Štular [65]). The table documents the anomaly’s identification, source data, and a preliminary morphological description of the anomaly, together with confidence scores for both the anomaly and its subsequent archaeological interpretation. Additional fields record the observational conditions (visibility and local vegetation density) that could affect detection, as well as the author and date of the mapping. Across the six campaigns, 162 anomalies were digitised in total, of which 100 carry an archaeological interpretation. The remainder record field boundaries, paths, recent disturbance, areas of retained surface moisture, and anomalies that could not be interpreted; these are retained in the overview of mapped anomalies in Supplementary Materials Table S3 but excluded from the counts reported in Table 4.

Table 4. Overview of the meteorological conditions, vegetation state, mowing regime and anomaly visibility across the six UAV campaigns at 't Huis ten Bosch. Daily values are from KNMI station De Bilt; antecedent windows end on the day before the flight, and the cumulative moisture balance is precipitation minus reference evapotranspiration over the window, with negative values indicating a deficit. The final block gives the number of anomalies carrying an archaeological interpretation recorded in each dataset, with those at good local contrast in brackets (Supplementary Materials Table S3); n/a means the sensor was not deployed, and 0 means it was deployed and nothing was recorded.

	9 Feb 2022	**2 Jun 2022**	**9 Sep 2022**	**15 Aug 2024**	**9 Sep 2025**	**30 Apr 2026**
Conditions on the flight day						
Mean temperature (°C)	8.9	13.7	15.8	21.2	12.6	14.2
Minimum temperature (°C)	8.3	4.6	12.9	16.4	6.9	7.0
Maximum temperature (°C)	10.0	19.6	18.2	25.5	15.8	20.2
Diurnal temperature range (°C)	1.70	15.00	5.30	9.10	8.90	13.20
Precipitation (mm)	0.8	0.0	1.6	0.0	18.2	0.0
Antecedent conditions						
Precipitation, 30 days (mm)	63.6	72.3	72.3	24.3	34.5	2.4
Moisture balance, 7 days (mm)	+38.9	−15.1	+8.7	−19.4	+5.8	−25.4
Moisture balance, 14 days (mm)	+54.3	+30.2	−10.7	−38.7	−7.2	−44.6
Moisture balance, 30 days (mm)	+54.4	−21.5	−23.1	−81.3	−54.7	−79.3
Mean DTR, 7 days (°C)	4.47	8.93	12.63	10.36	11.01	12.76
Mean DTR, 14 days (°C)	4.54	10.31	11.72	10.20	11.49	12.44
Mean DTR, 30 days (°C)	4.63	11.61	12.55	11.00	12.36	12.35
Vegetation and management						
Vegetation state	Dormant	Stressed, mown	Stressed (drought), mown	Stressed, recently mown, tyre tracks	Stressed (drought), unmown	Growing, unmown
Interval since mowing	c. 5 months	c. 4 weeks	c. 2 weeks	<1 week	c. 3 months	c. 7 months
Archaeological anomalies recorded (with good local contrast)						
Multispectral	3 (3)	4 (4)	5 (3)	3 (3)	9 (6)	12 (3)
Thermal	n/a	9 (8)	10 (8)	1 (1)	n/a	1 (0)
RGB	7 (6)	n/a	8 (8)	1 (0)	4 (4)	0
LiDAR	n/a	n/a	6 (5)	7 (7)	5 (5)	5 (3)

2.5. Meteorological Context Data

Weather conditions, both during the flight and in the days or weeks before it, as well as the broader seasonal pattern the flight falls within, affect the visibility of archaeological anomalies in remote sensing imagery [17,66,67].

Weather data for the site of 't Huis ten Bosch were therefore obtained from the Royal Netherlands Meteorological Institute (KNMI) weather station De Bilt (Station 260) [68], located approximately 22 km from the site. Daily records were retrieved for the period between 1 January 2022 and 1 June 2026, comprising mean, minimum, and maximum temperature (TG, TN, and TX, in °C), precipitation (RH, in mm), and reference evapotranspiration calculated using the Makkink method (EV24, in mm). These daily records describe the flight day as a whole and the period preceding it. Conditions at the moment of each acquisition, including the time of capture, the cloud conditions, and the moisture conditions, were recorded in the field for every flight and are reported per sensor in Supplementary Materials Table S1. The mowing regime was reconstructed in consultation with the landowner, who confirmed when the field had last been cut before each campaign. No record of exact mowing dates was kept, so for most campaigns this gives an approximate interval.

From these daily records, a set of derived variables was calculated for each acquisition date to characterise conditions in the days and weeks beforehand. Each was computed over three antecedent windows, covering the 7, 14 and 30 days preceding the flight; every

window ends on the day before the acquisition, so the flight day itself is excluded. The diurnal temperature range (DTR), the difference between daily maximum and minimum temperature, is reported both for the flight day and as an average over each window, and used as a contextual indicator of atmospheric temperature variability. Cumulative precipitation is the sum of the daily totals over a window, and the cumulative moisture balance subtracts from this the summed daily reference evapotranspiration across the same days, so that a positive value indicates a net water surplus and a negative value a net deficit. The cumulative moisture balance is used as an indicator of antecedent soil moisture conditions.

Of the variables obtained from the station, precipitation is the most sensitive to the distance between the station and the site, as rainfall can vary appreciably over a few kilometres, particularly where showers are localised. Individual daily totals may therefore not describe conditions at the field exactly, although cumulative totals over longer periods are less affected. These meteorological variables are used qualitatively, in combination with the per-campaign anomaly visibility analysis, to contextualise the conditions under which subsurface archaeological features were or were not visible in the UAV imagery of the site.

3. Results

3.1. 9 February 2022

The February 2022 campaign was flown under wet conditions, with standing rainwater visible across much of the field from the previous night's rain. The grassland was in a period of minimal winter growth, with the field last having been mown in September of the year before. Meteorologically, temperatures were mild for winter (mean 8.9 °C, range 8.3–10 °C) and showed a small diurnal temperature range, the lowest recorded in the dataset (Table 4; Figure 5, top left). The preceding month had been wet, with 63.6 mm of precipitation over the prior 30 days, most of it concentrated in the final two weeks (42.5 mm in the preceding 7 days alone), producing a pronounced moisture surplus in the weeks leading up to the moment of acquisition.

Only multispectral and RGB data were acquired during this campaign, flown at 11:20 and 12:00, respectively. No thermal imagery was collected due to heavy rain in the evening, and a LiDAR sensor was not yet part of the prospection arsenal at this stage. Metadata on all mapped anomalies can be found in Supplementary Materials Table S3.

The DEM derived from the RGB imagery provided a clear overview of the site's most prominent and already-documented anomalies (Figure 6, top left; Figure 7, top left). In the northwest of the study area (NB: the images are not north-aligned), a U-shaped depression 15 to 17 m wide was visible (ID 21), identified as the primary moat enclosing the castle grounds. The infill of this moat was not uniform, with localised height differences observable along its course. A slightly elevated section in the north and north-eastern corner (ID 22) was attributed to a greater concentration of rubble from the castle's destruction. At the centre of this enclosure, a raised area marked the site of the castle itself (ID 20), where a distinguishable linear anomaly, a wider U-shape with abutting north- and east-facing lines (ID 2 and 17), corresponded to the subsurface foundations of the castle's tower and walls. Approximately 25 metres east of the moat, a second linear depression running north–south was visible (ID 23), at the southern end of which a further, fainter linear depression ran perpendicular to it (ID 26). Due to its orientation and size, as well as the historical description of the castle possessing two moats, this anomaly has been tentatively interpreted as a secondary moat. In the north–east of the study area, a rectangular depression (ID 25) was identified, at the centre of which lay a lower-lying, cross-shaped region (ID 24). It was not possible to attribute a clear archaeological interpretation to these two anomalies.

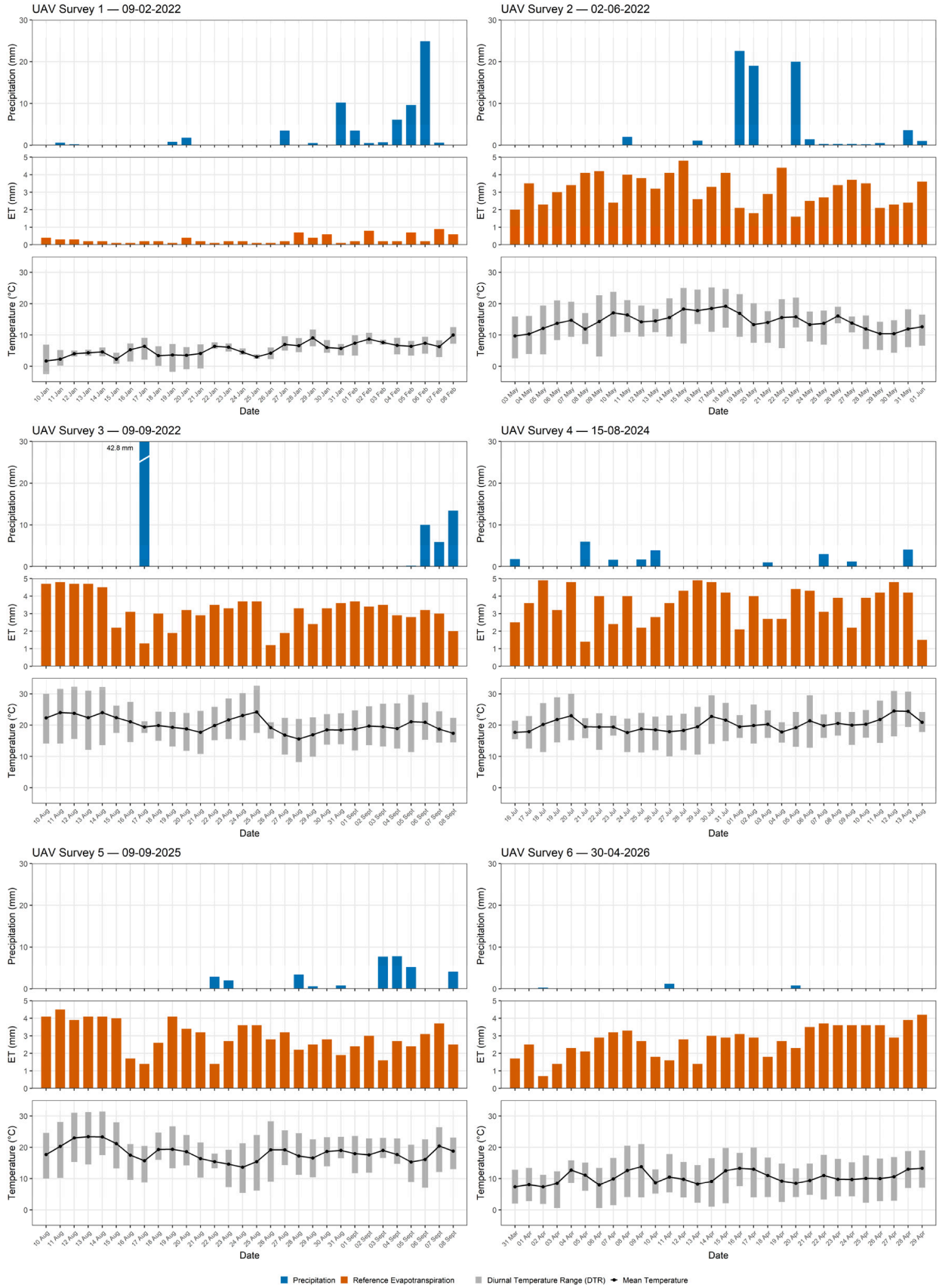


Figure 5. Daily precipitation, reference evapotranspiration, and diurnal temperature range with daily mean temperature, for the 30 days preceding each of the six UAV acquisition campaigns at ‘t Huis ten Bosch (Weesp), based on KNMI De Bilt station.

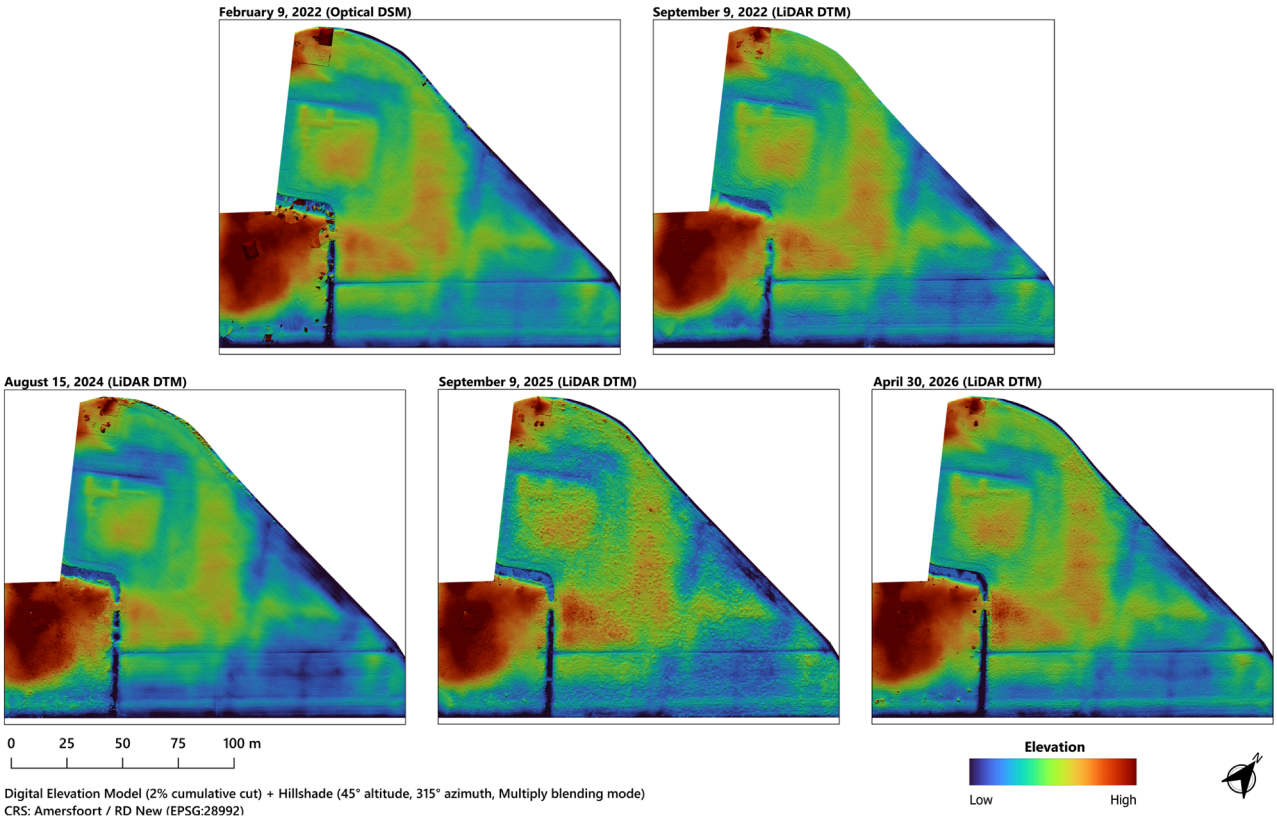


Figure 6. Digital elevation models of the site 't Huis ten Bosch, Weesp, across five UAV survey campaigns: 9 February 2022 (RGB DSM), 9 September 2022, 15 August 2024, 9 September 2025, and 30 April 2026 (LiDAR DTMs).

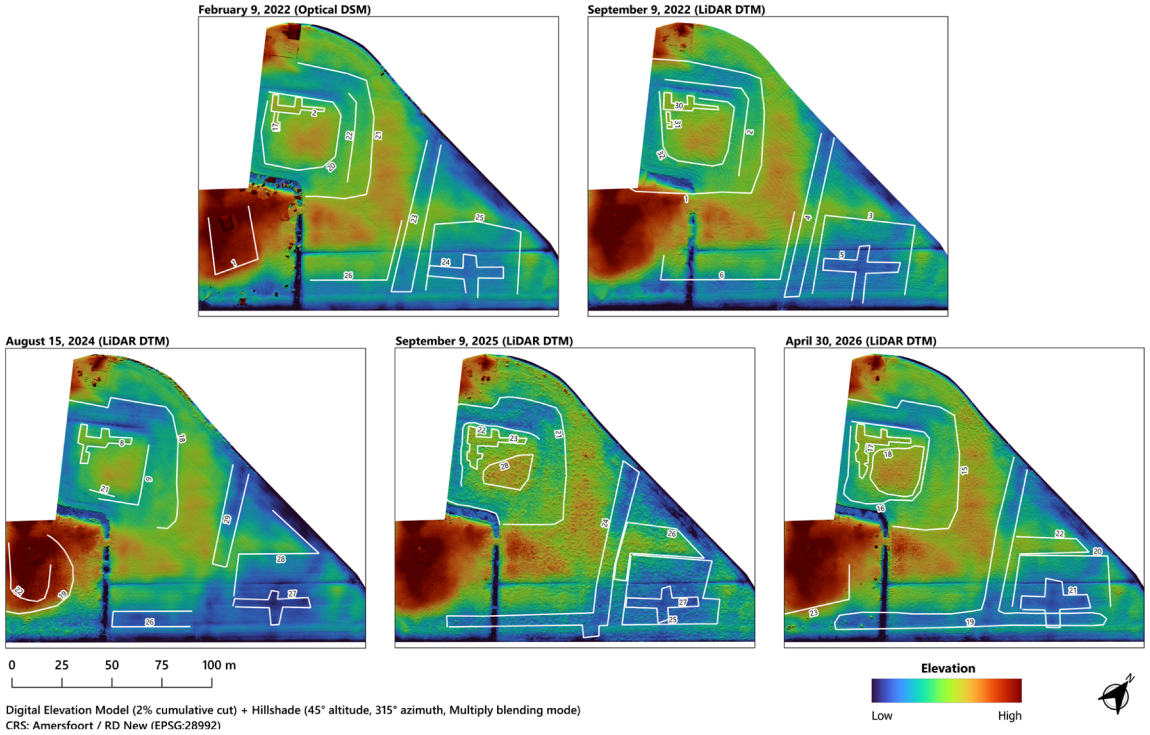


Figure 7. Digital elevation models of the site 't Huis ten Bosch, Weesp, across five UAV survey campaigns: 9 February 2022 (RGB DSM), 9 September 2022, 15 August 2024, 9 September 2025, and 30 April 2026 (LiDAR DTMs). The digitised anomalies are shown in white.

The RGB orthomosaic revealed a series of small, circular patches of dead vegetation, likely weeds, scattered across the castle grounds (Figure 8, top left; Figure 9, top left). These could not be convincingly related to anything archaeological. More notably, however, pools of water left by earlier precipitation outlined sections of several previously mentioned anomalies, including part of the tower and adjoining sections of the moat.



Figure 8. RGB orthomosaics of the site 't Huis ten Bosch, Weesp, across five UAV survey campaigns: 9 February 2022, 9 September 2022, 15 August 2024, 9 September 2025, and 30 April 2026.



Figure 9. RGB orthomosaics of the site 't Huis ten Bosch, Weesp, across five UAV survey campaigns: 9 February 2022, 9 September 2022, 15 August 2024, 9 September 2025, and 30 April 2026. The digitised anomalies are shown in black.

Multispectral imagery from this campaign showed generally poor visibility, with weak spectral contrast across the survey area (Figure 10, top left; Figure 11, top left; Figures A1–A9, top left). Three anomalies were identified in the GNDVI and MSAVI2 indices, all negative cropmarks. These were tentatively associated, at low confidence, with subsurface rubble present in the castle's primary moat (ID 28), rubble near the castle wall foundations (ID 29), and a linear anomaly (ID 27) stretching east–west through the course of the potential secondary moat.

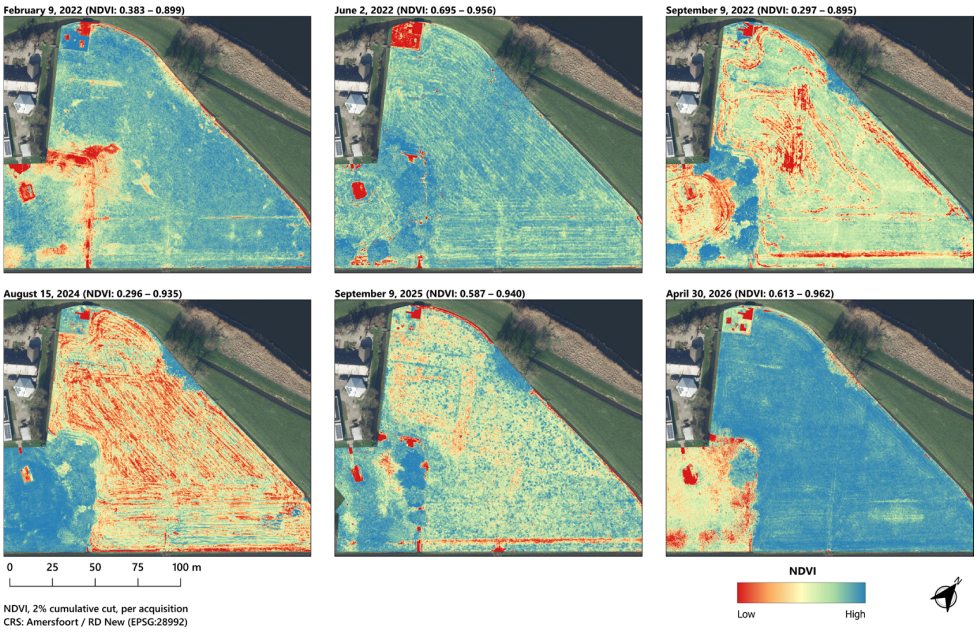


Figure 10. NDVI maps of the site 't Huis ten Bosch, Weesp, across the six UAV survey campaigns: 9 February 2022, 2 June 2022, 9 September 2022, 15 August 2024, 9 September 2025, and 30 April 2026. The displayed value range is given above each panel.

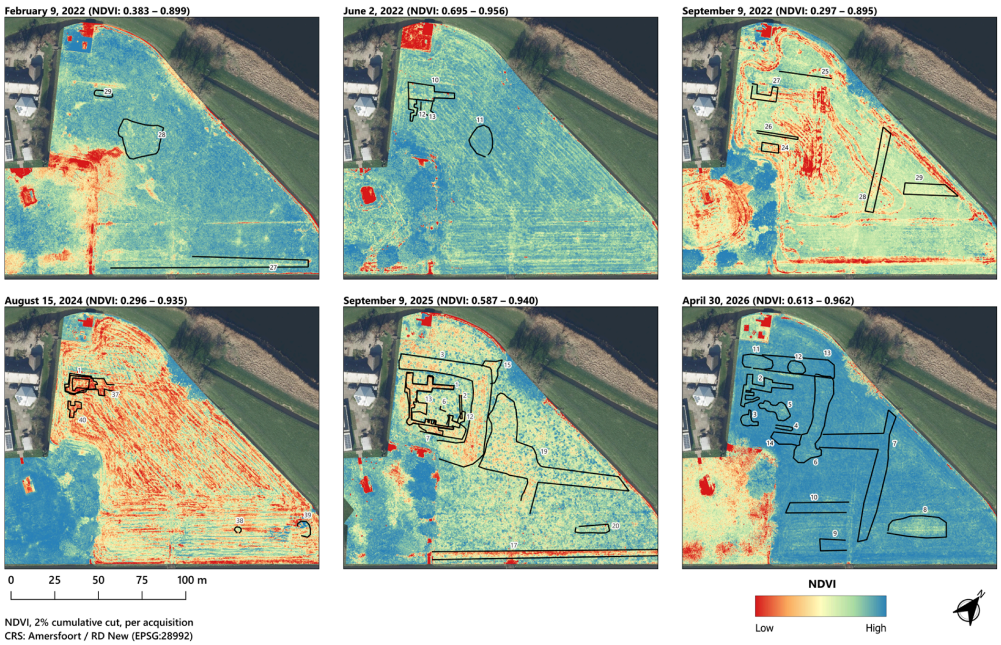


Figure 11. NDVI maps of the site, 't Huis ten Bosch, Weesp, across the six UAV survey campaigns: 9 February 2022, 2 June 2022, 9 September 2022, 15 August 2024, 9 September 2025, and 30 April 2026. The digitised anomalies are shown in black. The displayed value range is given above each panel.

3.2. 2 June 2022

At the time of the second campaign, conditions on site had shifted markedly from the wintry saturation of February. The grassland had been mown at some point prior to the survey; although an exact mowing date could not be established, from satellite imagery from the Dutch Satellietdataportaal [69] it was deduced that this activity took place somewhere between 4 March and 6 May 2022; the landowner recalled having the fields cut at the beginning of May, placing the survey roughly four weeks after mowing. This meant the vegetation was in a regrowth stage following mowing-induced stress. Meteorological conditions had also warmed considerably since the previous survey, with a mean temperature of 13.7 °C and a DTR of 4.6–19.6 °C on the day of acquisition, the largest day–night temperature swing during acquisition recorded across all six campaigns (Table 4; Figure 5, top right). Precipitation in the week directly preceding the flight was minimal (5.9 mm), though this followed a considerably wetter period further back, including a distinct rainfall event between 19 and 23 May (61.6 mm across those days, out of the 72.3 mm that fell in total in the entire month). In the week prior to flights, a moisture deficit of 15.1 mm was present.

In this campaign, both multispectral and thermal data were captured. No RGB imagery was acquired due to a technical issue with the sensor, meaning no RGB-derived photogrammetric elevation model was available for this survey either.

In the multispectral data, contrasts were improved slightly over the February 2022 recordings (Figure 10, top centre; Figure 11, top centre; Figures A1–A9, top centre). Looking beyond the striping left on the field caused by mowing, it was possible to see spectral contrasts present over the linear structure in the north-west of the castle terrain (ID 10 and 12). Note that these anomalies coincided largely with this structure but also show some additional details in its southernmost trace. A more ephemeral negative spectral mark was additionally present just below the tower foundations on the NDVI (ID 13), as well as an ovoid-shaped region of lower MSAVI2 values inside the area of the primary moat (ID 11).

The first thermal recording of these campaigns at Weesp showed relatively muted thermal contrasts across the entire study area but did reveal the outline of the tower with a good degree of clarity as a hot spot (ID 1) (Figure 12, top left; Figure 13, top left). Alongside this, several more linear features showing warmer signals were visible along the southern corner of the castle terrain, possibly relating to further, as yet undocumented, elements of the castle's internal layout (ID 2–7). Within the moats themselves, however, thermal contrast was largely absent, with only a faint, possible cold anomaly discernible along the course of the secondary moat (ID 9). In the wider area, only one other thermal anomaly was marked: a fork-shaped hotspot to the south-east of the primary moat (ID 8), for which no clear archaeological interpretation could be established.

3.3. 9 September 2022

In the two weeks before the UAV survey on 9 September 2022, the plot containing the research area had been mown extensively using a tractor. The tyre tracks of the vehicle and traces of the mowing remained distinctly visible on the surface at the moment of the campaign. The conditions on the day itself were generally warm (mean 15.8 °C, range 12.9–18.2 °C), but across the antecedent period, DTR fluctuated considerably over the preceding month, ranging from as low as 3.7 °C in mid-August to as high as 18.9 °C, before dropping to 5.3 °C on the day of the flight itself (Table 4; Figure 5, centre left). The preceding month had been largely dry, with a single substantial rainfall event on 17 August (42.8 mm). Little further precipitation fell until a cluster of rain days immediately before the campaign, between 6 and 8 September (29.3 mm in total), which shifts the moisture balance of the week preceding the flights into a surplus of 8.7 mm. A small amount of rain fell on the day

itself between the daytime and nighttime flights. All four sensor modalities were deployed during this campaign.

The new LiDAR-derived DTM for this campaign confirmed the same anomalies previously identified in the photogrammetric elevation model from February 2022, but at higher resolution, including the primary moat, the raised foundations of the castle's tower and walls, the secondary moat, and the unattributed rectangular depression and cross-shaped feature to the north-east (Figure 6, top right; Figure 7, top right).

The RGB imagery provided a clear overview of the tyre tracks and mowing marks left by land-use management activity at the site (Figure 8, top right; Figure 9, top right). Those areas most heavily affected by mowing coincided, for a large part, with anomalies already marked in previous campaigns. This applied both to raised areas (the remnants of the castle structure) and to some lower-lying areas, such as parts of the inner depression surrounding the castle itself. In both cases, these areas were largely devegetated, with bare soil showing through. Even with these interfering marks, several anomalies could be marked. These included a light negative cropmark in the shape of an inverted U (ID 8), oriented opposite to the previously identified tower foundations, as well as three further linear anomalies (ID 10, 11, 23) visible within the interior of the castle grounds.

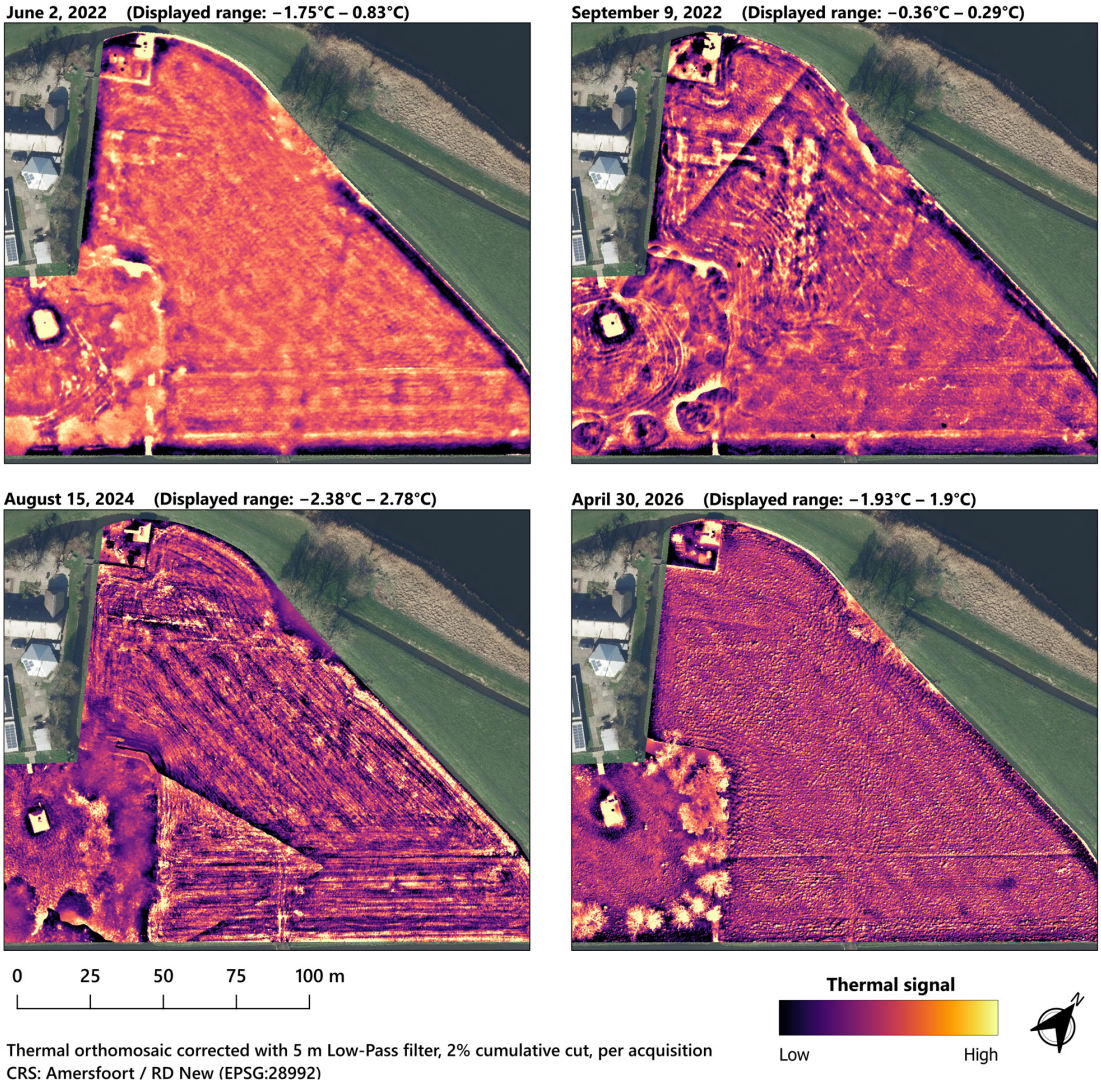


Figure 12. Thermal orthomosaics of the site 't Huis ten Bosch, Weesp, across four UAV survey campaigns: 2 June 2022, 9 September 2022, 15 August 2024, and 30 April 2026. The displayed value range is given above each panel.

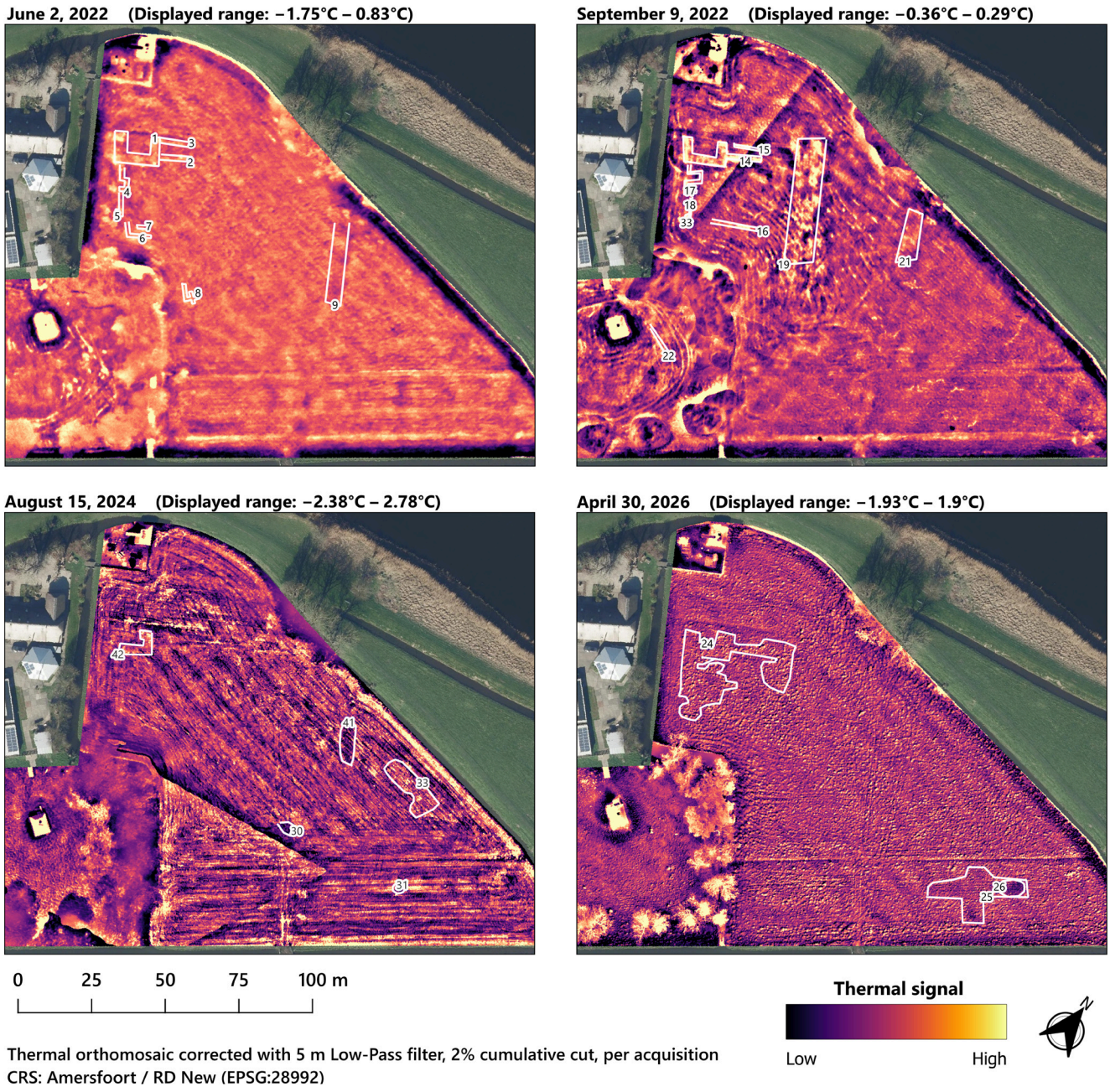


Figure 13. Thermal orthomosaics of the site 't Huis ten Bosch, Weesp, across four UAV survey campaigns: 2 June 2022, 9 September 2022, 15 August 2024, and 30 April 2026. The digitised anomalies are shown in white. The displayed value range is given above each panel.

The mowing marks introduced noise that made analysis of the multispectral imagery more difficult (Figure 10, top right; Figure 11, top right; Figures A1–A9, top right). Beyond the features already described in the RGB results, the north-west to south-east course of the outer moat (ID 28) was recognisable in the vegetation indices. So too was a negative cropmark running north-east to south-west (ID 29), though no definite archaeological interpretation could be assigned to this latter anomaly.

The thermography results from this campaign produced the strongest contrast recorded across all six surveys (Figure 12, top right; Figure 13, top right). Within the moat closest to the castle, concentrations of tractor tracks were visible in both the RGB and thermal imagery, but not all produced an equally strong thermal response. One rectangular section in particular (ID 19) showed a markedly stronger and more extensive thermal signal than

the tracks surrounding and leading up to the moat, despite comparable exposure of bare earth along those surrounding tracks. This anomaly has been tentatively associated with the presence of rubble used to backfill the moat following the castle's demolition, as its location broadly coincided with the section of the moat previously noted as having a slightly elevated infill in the February 2022 DTM data. In the northern end of the secondary moat, another patch of warmer temperatures (ID 21) was discerned. The castle structure likewise showed its clearest thermal expression of any campaign, coinciding with an area of exposed bare earth already visible in the corresponding RGB imagery. The warm-toned U-shaped outline (ID 14), interpreted as foundations of the tower walls, was joined by several other linear thermal anomalies (ID 17 and 18), together with a warm linear mark along the east side of the castle grounds (ID 16), possibly indicating an additional section of wall, and a shorter linear anomaly above the structure's northern side (ID 15). These last two were not previously visible in other imagery. Among the thermal anomalies from September 2022, the most notable was a semi-circular thermal signature 3.5 m in diameter at the southern corner of the castle terrain (ID 33), interpreted as the foundations of a small circular tower [70]. This anomaly was only perceivable in the thermogram, with no corresponding trace visible in the other sensor datasets from this campaign.

3.4. 15 August 2024

During the acquisitions in August 2024, the site entered its warmest and driest period in the dataset, with conditions on the day itself reaching a mean of 21.2 °C, the warmest single day recorded across all six campaigns (Table 4; Figure 5, centre right). Across the 30 days preceding the flight, evapotranspiration consistently exceeded precipitation on all but a handful of days, with only sporadic, generally minor rainfall (only 9.3 mm across the fortnight before the survey), resulting in a pronounced cumulative moisture deficit of 81.3 mm over the 30 days before the flight, the largest cumulative deficit recorded for any campaign. The DTR was largely wide and variable throughout this period, narrowing just before the flight due to the precipitation on 13 August. Less than a week before the flight, the grass was again extensively mown in multiple overlapping passes, leaving a dense, criss-crossing pattern of tractor tracks and cutting traces across the entire research area. As with the previous campaign, all four sensor modalities were deployed.

The LiDAR-derived DTM, while less plagued by the effects of the mowing, revealed no anomalies beyond those already identified in previous campaigns (Figure 6, bottom left; Figure 7, bottom left). One exception was an angled section of terrain to the north-east of the secondary moat's depression, marked here for the first time as an area of tentative archaeological interest (ID 28).

RGB imagery for this campaign showed no anomalies of note, beyond the mowing tracks and swath marks already described above (Figure 8, bottom left; Figure 9, bottom left). Multispectral results offered a slight improvement over the RGB data, though the vegetation indices still fell far short of the clarity seen in other campaigns for anomaly detection (Figure 10, bottom left; Figure 11, bottom left; Figures A1–A9, bottom left). Most indices, including NDRE, GNDVI, and NDVI, were largely saturated across the survey area. On the MSAVI2 map, the negative cropmark outlining the tower foundations (ID 36, 37) was still visible, as well as a possible cropmark (ID 40) corresponding to a small section of the south-eastern wall. Overall visibility of anomalies was, however, substantially reduced by the severity of the mowing.

Thermal imagery for this campaign was collected during daytime hours (the data was collected during daytime hours to accommodate a scheduled demonstration). The resulting data suffered from extensive alignment issues during photogrammetric processing, producing pronounced artefacts across the orthomosaic, potentially caused by increased

thermal drift due to accelerated sensor heating during operation on the warm day (Figure 12, bottom left; Figure 13, bottom left). Combined with the disruption caused by mowing, this made it difficult to distinguish anomalies with confidence. Still, some anomalies were visible. A faint hotspot (ID 42) corresponded to the foundations of the tower, though the characteristic U-shape identified in prior campaigns was considerably less distinct than in other campaigns, and the western and northern walls, visible in earlier campaigns, could hardly be distinguished. Several smaller thermal anomalies of uncertain origin were present (ID 30, 33), including a circular cold anomaly (ID 31) in the centre of the cross-shaped anomaly in the north-east corner of the plot. No archaeological relevance could be attributed to these. A cooler, oval-shaped anomaly (ID 41) was additionally noted in the secondary moat, though this is considered a low-confidence, likely spurious signal given the extent of noise affecting this campaign's data overall.

3.5. 9 September 2025

In the weeks leading up to this campaign, the site had been in a largely dry stretch, with evapotranspiration outpacing rainfall for weeks on end until a series of wetter days from 3 September onward, building to the single wettest day recorded anywhere in the dataset, 18.2 mm, on the day of the survey itself (Table 4; Figure 5, bottom left). Still, this late rainfall was not enough to offset the preceding dry weeks, and a cumulative moisture deficit of 54.7 mm remained over the 30 days before the flight. Temperature swings had also settled down by this point: DTR, which had been as wide as 20 °C in mid-August, narrowed considerably through the second half of the month, and conditions on the day of acquisition were mild overall, warmer during the day but cooler by evening (mean 12.6 °C, range 6.9–15.8 °C). For this campaign, mowing was deliberately postponed until after the survey, allowing the grassland to reach the peak of its vegetation cycle at the moment of acquisition. Unfortunately, due to the unceasing rain, it was impossible to acquire thermal imagery on this date. RGB, multispectral, and LiDAR data were still successfully captured.

Compared to the LiDAR-derived DTMs of prior campaigns, this survey captured a distinctly mottled surface texture across the research area for the first time (Figure 6, bottom centre; Figure 7, bottom centre). A comparable pattern was also clearly visible in the RGB imagery and was caused by small-scale variations in vegetation height across the sward.

Beyond this, the RGB orthomosaic already showed extensive areas of contrasting vegetation health, including around the castle (ID 8, 11) and moat (ID 9), though these patterns stand out with even greater clarity in the corresponding multispectral indices, discussed below (Figure 8, bottom centre; Figure 9, bottom centre).

Indeed, this campaign's multispectral imagery showed the clearest vegetation-mark visibility of any survey to date, though this overall clarity was somewhat tempered by speckling caused by the vegetation's own patchiness, which introduced a degree of visual noise across the indices and made some of the finer anomalies more difficult to discern against the surrounding texture (Figure 10, bottom centre; Figure 11, bottom centre; Figures A1–A9, bottom centre). Nonetheless, the moat surrounding the castle terrain remained distinctly traceable on the indices, with distinguishable negative spectral marks visible along its north-east and north-west sections, possibly related to the presence of archaeological remains used to fill in the castle. In the north corner of this moat, a previously unidentified spectral mark (ID 15) was also present, appearing to extend beyond the moat's depression as seen in the LiDAR DTM. On the castle island itself, the foundation walls, including the tower, remained clearly traceable (ID 1, 13) and were now joined by several further features in the south-east, possibly relating to internal buildings or additional elements of the perimeter wall. One such element, a semi-circular spectral mark in the southern corner, coincided with the thermal anomaly identified in September 2022, further supporting the presence of

a small circular tower having been part of the former structure. Signals were comparatively weaker at the northern corner, though some negative cropmarks (ID 2, 12) could still be distinguished there, effectively bringing the perimeter closer to a fully continuous outline than in any previous campaign. Beyond the castle, a larger, though more diffuse anomaly showing up as an area of poorer growth (ID 19) crossed the outer moat and extended toward the inner enclosure, corresponding to the same elevated area first identified in the LiDAR data of 2024. The archaeological interpretation of this feature, though uncertain, is that it could relate to a remnant of a former route towards the castle.

3.6. 30 April 2026

The final UAV survey at the site took place during spring of 2026. The field had last been cut in September 2025, some seven months before, and the grass at the site was in a state of active, uniform growth across the entire site. Differences in vegetation height noticed during the previous campaign were much less apparent. Flights took place on a relatively warm and pleasant day (mean 14.2 °C, range 7–20.2 °C), with the second widest day–night temperature swing recorded across the surveys (13.2 °C DTR) (Table 4; Figure 5, bottom right). These wide ranges in diurnal temperature were present throughout the entire preceding period as well. What had preceded the survey was a remarkably dry stretch: barely any rain fell in the month before it, just 2.4 mm in total, with only 0.8 mm falling in one small event ten days before the flight. The cumulative moisture deficit, 79.3 mm across the 30 days prior to the flight, was accordingly high, second only to the extremes of August 2024. All four sensors were flown during this final campaign. In the LiDAR and RGB data, no previously unidentified anomalies were detected.

Multispectral results were fairly flat once again, with relatively low contrast throughout. Some anomalies were nonetheless registered around the castle terrain, including the angled, linear spectral marks (ID 2) corresponding to the foundations that have produced topographic expressions across all campaigns, though these appeared more diffuse here than in other surveys (Figure 10, bottom right; Figure 11, bottom right; Figures A1–A9, bottom right). Other features found on the indices again included a semi-circular spectral mark (ID 3) in the southern corner and a short linear mark (ID 4) in the south-eastern corner of the castle terrain, along with a diffuse negative cropmark (ID 5) at its centre. Outside the castle, the primary moat produced more negative spectral signatures (ID 6, 11, 12) along its northeastern and northwestern course. A vague positive cropmark (ID 7, 14) ran along almost the entire secondary moat, also branching transversely towards the primary moat. In the western corner of the research area was a sharply negative feature (ID 8), corresponding to the location of the cross-shaped depression visible in the LiDAR data, but whether it is of land-use or archaeological origin remains unclear.

The thermal orthomosaic for this campaign showed surprisingly little contrast, despite meteorological conditions that might otherwise have been expected to favour a strong result (Figure 12, bottom right; Figure 13, bottom right). Only a faint warmer signature on the castle island (ID 24) hinted at the presence of any archaeologically related anomalies. The distinct negative cropmark in the western corner also appeared as a cool spot in the thermal data (ID 25), preserving the cross-shape previously observed in the DTM. At its northern end, a circular cold anomaly (ID 26) was also visible.

4. Discussion

4.1. Comparison of the Prospection Results

This section compares the anomalies identified across the multi-temporal UAV data with the subsurface record already established by the 2022 geophysical survey and coring campaign, working through the site's principal features in turn: the primary moat, the

secondary moat, and the central tower and walls. Each feature showed a distinct signature across the UAV datasets, revealing where the drone data aligns most closely with the geophysical and coring results, and where it adds detail, or occasionally misses detail, that those earlier surveys alone could not provide (Table 5). This comparison is interpretative: it draws on all available evidence to establish what the features are and is distinct from the assessment of detectability in Section 4.2, which rests only on whether anomalies were discernible within each dataset.

Table 5. Sensor-by-campaign visibility of the principal archaeological features at 't Huis ten Bosch. R = RGB, M = multispectral, T = thermal, L = LiDAR; capitals indicate that the feature was registered at good local contrast in that dataset and lowercase at poor contrast (Supplementary Materials Table S3). A dash means the feature was not recorded in that campaign. The final column gives the independent subsurface evidence for each feature from the 2022 geophysical survey [31] and coring campaign [32].

Feature	9 Feb 2022	2 Jun 2022	9 Sep 2022	15 Aug 2024	9 Sep 2025	30 Apr 2026	Attested by
Primary moat	R	-	m L	L	R M L	m L	Coring, geophysics
Secondary moat	R M	t	R M t L	L	R m L	m l	Coring, geophysics (phasing unresolved)
Tower/walls	R M	M T	R M T L	r M T L	M L	M t L	Coring, geophysics
Rubble/demolition	r M	M	T l	-	M L	M l	Coring, geophysics
Castle island/terrain	R	-	L	-	R L	L	Geophysics

The moat, in particular, was traced across nearly every campaign, most sharply in the September 2025 multispectral indices. Throughout the multispectral data, the moat consistently produced negative rather than positive cropmarks, a somewhat counterintuitive result given that ditch features typically produce the opposite signature: positive cropmarks driven by the additional moisture and nutrients retained in ditch fill, which in turn support more vigorous plant growth above them [27,71]. Instead, vegetation directly above the moat was comparably stunted, implying the composition of the fill is less favourable to plant growth than the surrounding ground. This pattern is consistent with the evidence for intentional backfilling identified by both earlier surveys. The coring campaign found deposits of rubble from the demolished castle at about 25–50 cm below the surface within several boreholes along the moat's course [32], while the geophysical survey recorded relatively high magnetic contrast and low soil conductivity in the moat, both attributable to the presence of subsurface rubble containing fired building materials such as brick [31]. The presence of this material diminishes the water and nutrient availability, resulting in negative cropmarks [72]. The use of material from the castle structure being used to backfill parts of the terrain can be further corroborated by the September 2022 thermal orthomosaic. This showed warm signals along the moat, concentrated at locations of exposed bare earth left by mowing. Not every patch of exposed bare earth responded equally, however: ID 19's thermal signal was considerably stronger and more extensive than surrounding areas of similarly bare ground, suggesting that exposure alone does not account for its strength. A plausible explanation lies in a difference in the thermal properties of the material filling the moat at this location. Dense brick and rubble fragments typically carry a higher thermal inertia than the surrounding soil, allowing them to absorb and store heat over the course of the day and release it more gradually as ambient temperatures fall toward evening [20,73]. By the time of the evening acquisition, the lower-inertia surrounding soil had already begun cooling faster than the more thermally massive rubble, which remained comparatively warm, producing the anomaly recorded at ID 19. No direct measurements of the fill material's

density, moisture, or compaction are available to confirm this mechanism at this specific location, however.

The existence of a possible secondary moat remained unresolved by both the geophysical and coring surveys [31,32]. Both identified traces of a ditch-like feature, with a fill consisting of clay and building rubble, but neither could confirm its connection to the castle. While the remote sensing data could not clarify the exact phasing of this feature, its course could be traced across several campaigns. Its north–south course was most clearly visible in the elevation data. Interestingly, an angled section of raised terrain to the north-east (ID 28 in August 2024) appeared to cross the depression. A faint warm thermal trace was already visible along its northernmost end in June 2022, followed by a clearer negative cropmark (ID 28) and a corresponding warm thermal anomaly (ID 21) in September 2022. This combination closely resembled the signature already attributed to subsurface building material in the primary moat. This same course, however, produced a positive cropmark in April 2026 (ID 7), the inverse of the signature recorded in September 2022. This reversal complicates a straightforward archaeological reading of the feature, and most likely reflects differences in the specific conditions under which each campaign was recorded rather than any change in the feature itself, consistent with the broader influence of season and vegetation state on cropmark visibility discussed in Section 4.2.

Beyond the moats, the castle's central structure also proved to be a reliable feature on the remote sensing data. The geophysical survey had already established a coarse outline of the tower's original plan, along with a rough delineation of the surrounding walls, through the magnetic contrasts and low soil conductivity in this area [31]. The UAV data reproduced and refined this outline in detail. The tower itself, located in the western corner of the castle terrain, produced the most prominent of these anomalies, with a clear topographic expression visible on the drone-derived elevation data. On all thermograms of the site, this rectangular feature showed up consistently as an area of relatively high thermal emissions, even in campaigns where the field was covered by a uniform layer of vegetation, such as in April 2026, where, though fainter, the anomaly could still be made out. In the multispectral imagery, this same feature also reliably produced negative cropmarks which were discernible in the vegetation indices in every campaign except for the February 2022 recordings. As with the moat, this combination of a distinct thermal signature and vegetation-suppressing cropmarks is consistent with the presence of buried structural remains beneath the tower and walls. This aligns with both the site's documentary and geophysical record. While most of the castle structure was removed following its final destruction, the poured foundations were reportedly left in situ and only fully removed in 1925 [30]. The geophysical survey had already suggested that this later removal was incomplete [31]. Now, based on the strength and consistency of the anomalies in the drone remote sensing data, this inference is strengthened, indicating that substantial foundation material remains in situ beneath the tower and walls.

The geophysics showed rectangular walls enclosing this terrain [31], and it is these abutting walls that were also recorded in the remote sensing data. In the successive multispectral and thermal campaigns, it was possible to map the stretches of wall on the north-western, south-western, and south-eastern sides. An anomaly possibly relating to the section of wall on the north-eastern side of the terrain was only visible once, in the multispectral data of September 2025. The fact that this section is less consistently expressed than the other three sides in the spectral data might suggest that it only became detectable under the particularly favourable vegetation and moisture conditions of that specific campaign, or alternatively, that this section of the wall and its foundation was more diligently removed for re-use following the castle's destruction.

Besides confirming the other prospection results, the drone data also revealed structural detail absent from the geophysical record. One example is the small circular thermal anomaly identified in the southern corner of the castle terrain in September 2022, corroborated by matching spectral marks in the same location in the September 2025 and April 2026 vegetation indices. This feature has been interpreted as a corner tower [70]. Besides the tower, other examples are the less well-defined rectangular anomalies which appeared alongside the south-eastern and south-western stretches, possibly traces of outbuildings or annexes associated with the motte (ID 7 and ID 13, September 2025). The inverse was also the case: one of the more distinct wall details interpreted in the magnetometry and EMI data, the northern of the two parallel lines emanating from the tower's northern edge, was only marked in the thermal maps from June and September 2022, but invisible in all other drone data.

Together, these two discrepancies between the earlier geophysical survey and the drone-derived results show that no single prospection technique, applied on its own, would have produced the full overview of the subsurface archaeology obtained at the site of 't Huis ten Bosch. Other multi-sensor UAV surveys report much the same [22,26,27]. Brooke and Clutterbuck [27] found thermal providing most of the archaeological information at one of their two English sites and multispectral at the other, and recommend RGB, multispectral and thermal as a minimum set of sensors to use. Salgado Carmona et al. [22] found the same sensors picking out buried structures clearly in one part of a site and poorly in another, imaged on the same day under identical conditions, a difference which they ascribe to the depth and configuration of the archaeological deposits.

The need to combine methods extends to coring. Still the most commonly applied prospection method in the Netherlands, it remains fundamentally limited to point samples, unable to trace a feature's spatial extent the way the geophysical and UAV surveys did here. Yet it was coring that provided the direct stratigraphic sampling needed to interpret what these spatially continuous anomalies actually represented. Greater integration of geophysical and remote sensing methods alongside coring within the KNA-defined prospection workflow would thus yield a more complete and reliable picture of subsurface archaeology than any one method pursued in isolation.

4.2. Contextualising Anomaly Visibility

The comparison that follows concerns detectability alone: whether an anomaly was discernible within a given dataset, independent of its archaeological interpretation. Across the six campaigns, the visibility of the anomalies on the multispectral and thermal data followed distinct and only partially overlapping patterns, and neither tracked any single meteorological variable in isolation. The multispectral data with the poorest visibility of archaeological features came, expectedly, from the February 2022 campaign. With the site in a period of minimal winter growth, the largest moisture surplus of all visits, and no recent mowing or other management activity to introduce disturbance, the grass cover was in a broadly uniform, dormant state across the entire site. The kind of localised contrasts in vegetation health that multispectral indices are built to detect had therefore not yet had the opportunity to develop. This result is in contrast with Bennett et al.'s [74] results from the calcareous grassland of Salisbury Plain in England, where a January capture, taken while the vegetation was dormant, revealed more archaeological features than imagery collected in May at peak growth. Though no meteorological data are reported by the authors allowing for a comparison of antecedent moisture conditions, Weesp shows the opposite pattern, which could plausibly relate to the different soil contexts at the site as much as to the season: Salisbury Plain's calcareous grassland is free-draining, while Weesp's clay subsoil tends toward waterlogging. The RGB imagery reflects this, with standing water left

by the preceding night's rain pooled unevenly across the site, outlining sections of the tower and the northern moat where infiltration evidently differed from the surrounding ground.

A comparably weak result was recorded in April 2026 across both the multispectral and thermal sensors, despite meteorological conditions that, on paper, appeared favourable to produce contrasts. A substantial cumulative moisture deficit had built up over the preceding month, the second largest recorded across the dataset, and the day of the flight had a pronounced diurnal temperature range. The multispectral result closely mirrors Emaus [15] findings from a comparable Dutch grassland site near Ramele, where four UAV multispectral surveys were flown across the 2022 growing season to track vegetation marks over a known archaeological feature in relation to the timing of mowing. That study's April dataset showed no clear vegetation marks despite similarly dry conditions, a result attributed to the grass's early phenological stage and correspondingly limited biomass. At Weesp, the grass was likewise still early in its active growth cycle, with plenty of moisture still in the plants themselves, and simply had not grown enough yet for the deficit to show up as any real difference in vegetation health across the site.

The April 2026 thermal result is harder to account for, given the combination of dry antecedent conditions and a wide diurnal swing, a combination often associated with strong thermal contrasts [20,24]. A plausible explanation still lies in the vegetation itself: with the grass still in active early-season growth, the thermal sensor was likely registering the surface temperature of the grass itself, with the soil screened beneath it. A moist, actively growing sward dampens the temperature swing a bare or sparsely vegetated surface would otherwise show, through the water it holds and the heat carried away as that water transpires [9].

The idea of an optimal growth stage comes largely from work on fields with annual arable crops, such as cereals, where visibility can be tied to a defined phenological stage: Agapiou et al. [66] locate the optimum in a fifteen-day window at the beginning of the boot stage, and Moriarty et al. [75] found marks at the site of Ravenshall, in Scotland, becoming separable from June onwards across a series flown between April and July. A perennial, repeatedly mown sward offers no comparable anchor, having no single annual maturation and a development reset several times a year by cutting. Emaus [15] argues that mowing is itself a primary driver of vegetation mark visibility in grassland contexts: none of the vegetation marks in that study was visible while the grass was at peak growth, and all appeared only in the weeks following mowing, when it is suggested that the physiological stress of cutting, combined with the temporary levelling of height and biomass across the field, allows any pre-existing subsurface variability to register more clearly in the crop's response. That study's own August dataset, recorded under comparably dry, recently mown conditions, was its clearest result of the growing season on this basis.

The survey at 't Huis ten Bosch in August 2024 was recorded under closely comparable conditions: the largest 30-day cumulative moisture deficit of the dataset, high daytime temperatures, and following recent mowing. The visibility of anomalies in this campaign was, however, severely limited. Two things could possibly explain this difference. First, the field in Weesp had been mown extremely coarsely, with repeated, overlapping passes churning up much of the ground and leaving bare soil exposed in places, resulting in very noisy vegetation indices. Second, the flight took place less than a week after cutting, potentially leaving too little time for any differential regrowth to develop before capture. The thermal data for this campaign was also of limited use, though for a more straightforward reason: due to operational reasons, the flight was conducted during daylight hours rather than after sunset. Some anomalies, including the tower, could still be tentatively identified in the imagery, suggesting a daytime capture is not entirely without value in a pinch, but the difficulties encountered in photogrammetrically processing the dataset make it a poor substitute for an evening flight. Both of these difficulties are familiar from the recent

literature. Hall and Ernenwein [41], who flew nineteen thermal surveys across a year at a mown cemetery in Virginia, found that acquisitions made soon after cutting were compromised by mowing lines and clumps of dead grass, which introduced anomalies of their own, and that daytime flights fared poorly as uneven solar heating and the shadows cast across the ground obscured the subsurface signal. Ciccone [40] reports the opposite on timing, finding mid-morning and mid-afternoon flights over wheat more productive than either pre-dawn or post-sunset acquisitions, with the thermal data outperforming the multispectral and RGB imagery flown the same day. The difference seems to lie in the crop: under dense wheat in advanced growth, variations in root-zone moisture above buried features register through transpiration during the day, while the grassland at 't Huis ten Bosch offers no comparable daytime signal and the useful window stays after sunset. August 2024 was flown in the early afternoon, and it reproduced both of the problems Hall and Ernenwein describe.

June 2022 offers more mixed results. The relatively dry week in which the recordings took place was preceded by heavy rainfall, and mowing had occurred several weeks earlier. Still, multispectral contrast remained largely limited to only the most prominent castle traces. This mirrors the June dataset of [15], recorded that same year under similarly wet and mild conditions following an earlier mowing event, where cropmarks were likewise only faintly visible, attributed to residual soil moisture from preceding rainfall supporting a fairly uniform regrowth across the field and muting the sharper contrast that fresher post-mowing stress might otherwise produce. That the tower and walls remained visible at Weesp despite this muted contrast is consistent with these being the most robust anomalies at the site, recurring across nearly every campaign regardless of conditions. More subtle features, such as the secondary moat, appear to require a sharper contrast than June 2022 offered to register at all. The thermal data was comparatively more informative than the multispectral results from this campaign, tracing the stone wall foundations. This came under a relatively dry week following a wetter late May, and the widest diurnal temperature swing recorded across the dataset. It may be that this transition itself supported the contrast observed, as the subsurface materials and the surrounding soil matrix, each with differing thermal inertia, would have responded to the changing conditions at different rates [20,76].

September 2022 stands as the strongest campaign for thermal contrast across the entire series, despite extensive tractor-track disturbance from mowing carried out two weeks before the flight. The multispectral result was more modest, though stronger than August 2024, where mowing occurred less than a week before capture; the longer interval here left more time for differential regrowth to develop before the survey, a timing more consistent with the pattern identified as favourable for cropmark visibility in grasslands [15]. Drought stress alone does not appear to explain the result here either. The 30-day cumulative moisture deficit recorded ahead of this campaign was far more modest than those preceding August 2024 or April 2026. Much of the preceding month had been dry, interrupted only by a single substantial rainfall event roughly three weeks before the flight, before a further cluster of wetter days closer to the survey date. The clearest result in the dataset, once again, did not follow the most extreme drought, a pattern also noted by Kozioł et al. [17], who found archaeological visibility in satellite imagery to peak under moderately dry conditions and fall away under severe drought, with predictive accuracy highest while moisture conditions were fluctuating.

A similar dynamic to June 2022 may explain the thermal result, and here the effect appears more pronounced still, with rainfall in the days before the flight, following a largely dry preceding stretch, alongside a marked cooling trend leading into the day of acquisition. As with that earlier campaign, the shift from one set of conditions to another, more than either state on its own, may have been what mattered here, allowing shallow buried material

and the surrounding matrix to diverge briefly in temperature before settling into a new equilibrium. That this campaign produced the clearest thermal signal recorded anywhere in the dataset suggests such transitional conditions may be considerably more conducive to the detectability of thermal anomalies than a prolonged dry or wet spell on its own. Hall and Ernenwein [41] place September near the top of their own series, recording their second-highest nighttime contrasts there across a year of flights at a mown cemetery, with the cooler months consistently weaker as shallow soils gave up the summer's accumulated warmth. Shorter shifts of the kind seen here would be working on whatever heat the season has left in the ground.

September 2025 produced the clearest multispectral expression of the castle plan recorded anywhere in the dataset. Clarity here concerns the coherence of the features the marks describe, and not the number of anomalies recorded, as while April 2026 carries more individual records (Table 4), a larger share of these trace parts of the same features. A substantial cumulative moisture deficit had built up over both the preceding two weeks and the preceding month, coinciding with the grass approaching the natural end of its growing cycle. Under these conditions, differences in vegetation vigour across the site appear to have become considerably more pronounced than in earlier campaigns. The resulting imagery showed a distinctly heterogeneous crop mark pattern across the sward, even within features, a pattern consistent with the kind of "salt-and-pepper" heterogeneity described by Materazzi et al. [77], where individual plants growing under otherwise similar conditions can follow markedly different phenological trajectories. This, however, did not prevent the moat, tower, and wall foundations from producing their clearest signatures of any campaign, nor did it prevent several previously unrecorded features from emerging for the first time. The strong detectability of anomalies in the multispectral data here presents a different picture from the pattern proposed by Emaus [15]. Cutting of the grass was deliberately postponed until after the survey, allowing the grassland to reach the peak of its growth cycle at the moment of acquisition. This diverges from the findings at the site in Ramele, where visibility consistently followed mowing, and no marks were recorded while the grass was at peak growth. Whether this difference comes down to the grass composition at each site, the severity of the late-season moisture deficit, or whether cumulative stress is not, in fact, the main driver of cropmark visibility here at all, remains an open question, but it does suggest mowing is not the only path to good visibility of archaeological anomalies in grassland environments. Hall and Ernenwein [41] reach a comparable position from the thermal side, advising that surveys be flown before the field is cut, since mowing introduces noise of its own. Our September 2025 campaign was flown in precisely those circumstances, and suggests that grassland can carry strong vegetation marks with no recent cutting at all.

4.3. Limitations and Future Research

Several limitations of this study should be acknowledged. Firstly, the six acquisition campaigns, while spanning more than four years, remain a limited number of observations. Both the phenological cycle of the grassland and the timing of mowing appear to have shaped visibility across the present dataset, and the six campaigns sample neither evenly. No thermal acquisition in the series falls in midsummer, the point at which Hall and Ernenwein [41] record their maximum nighttime contrast, making a July evening flight the most obvious addition to any future campaign plan at the site. Secondly, and related to this, not every sensor modality could be deployed during every campaign, owing to weather conditions and operational constraints, and the platform and all three sensor types were replaced at some point over the four years, so hardware generation and environmental conditions cannot be completely separated within six campaigns. The outcomes do not follow the hardware, however, as the strongest thermal results came from the June and

September 2022 campaigns, recorded with the XT2 at 22.9 and 16.6 cm, while the finest thermal dataset in the series, April 2026 with the newer H30T at 4.0 cm, produced among the weakest. The multispectral series runs the same way, with the two clearest campaigns recorded at 6.4 and 7.2 cm against 3.4 cm for the weakest. What the clearest campaigns share is the state of the field; in both cases, unmown vegetation under a pronounced antecedent moisture deficit, and not the generation of the sensor. Thirdly, meteorological data for this study were drawn from a single KNMI weather station, De Bilt, the closest one to the site but still some 22 km removed. While broad regional patterns, such as average temperature and precipitation trends, are unlikely to differ substantially over this distance, more localised effects, such as the intensity of individual rainfall events, may not always be fully captured by a station at this distance. Fourthly, the optimal conditions for anomaly detectability identified across the six campaigns are, to some degree, specific to this site. As the comparison of optimal visibility in other grassland sites in Section 4.2 shows, the relationship between meteorological conditions, land management, and anomaly visibility at 't Huis ten Bosch broadly matches what has been reported elsewhere, though not always. Soil composition, hydrology, and vegetation cover vary considerably even between individual grassland sites, so the results here should be read as site-specific rather than a general model for grassland visibility.

A further limitation concerns the mapping itself. The UAV outputs for each campaign were mapped independently by three interpreters and the results subsequently reconciled, but only the reconciled mapping was retained, so the degree of agreement between them cannot be quantified retrospectively. All interpreters were moreover familiar with the site and with the 2022 results, which, while appropriate for archaeological interpretation, means the detection step cannot be described as blind. Finally, the comparative framework used here rests on independent but incomplete subsurface evidence. Definitive confirmation of the archaeological character, date, and material composition of the features identified, particularly those newly recognised in the UAV data such as the circular anomaly in the southern corner of the castle terrain, would require more invasive methods such as trial trenching or excavation.

Building on this study, several directions for future research can be identified. At the site-scale, installing a dedicated local weather station, rather than relying on a distant regional one, would allow more local meteorological variables to be captured, variables that could not be considered in detail in this study. Wind speed, for instance, has been linked to increased soil evaporation and plant water stress, and was found to correlate with anomaly detectability in a satellite-based machine learning study of archaeological site visibility [17]. Complementing this with direct, in situ soil moisture monitoring would allow the moisture-driven explanations proposed throughout this paper to be tested more rigorously still. Ground surface temperature and the heat exchanged with the soil below could be monitored in the same way, allowing the energy balance at the surface to be observed directly where this study could only approach it through air temperature. Work along these lines is already underway at the site of Veldhoven in the Netherlands, where soil monitoring sensors and sedimentological sampling are being combined with drone-based remote sensing data to establish the physical and pedological reasons behind feature visibility, in this case in an open-excavation context [13]. A similar approach could also be implemented here in future campaigns at 't Huis ten Bosch. Future work could also explore UAV hyperspectral imaging, a method which is currently in a much more experimental phase [78], but could potentially be used to discern subtle soil marks or traces of vegetation stress signatures as demonstrated in satellite applications of the technique [67,79].

Drawing these threads together, the study points towards a minimum framework for comparative work of this kind in grassland and pasture environments. Campaign

distribution is the first requirement, and based on the provisional evidence from this site: at least one acquisition per season, two of them in the growing season and timed to bracket a mowing event, with an evening thermal flight in midsummer, a window left unsampled here. The second concerns sensor coverage, as no single modality at 't Huis ten Bosch registered every feature class, and RGB, multispectral and thermal data in every campaign, with an elevation model acquired at least once, would allow such differences to be assessed consistently between sites. Third, acquisition and processing parameters should be reported per campaign and per sensor, including the radiometric settings and drift correction applied to thermal data. The Supplementary Materials accompanying this paper are offered as a template. The in situ monitoring described above forms the fourth requirement. Finally, the criteria by which anomaly contrast and interpretive confidence are judged should be fixed before mapping begins and deposited alongside the mapping, as they are here (S3). Having several interpreters apply them independently of the reference material would allow inter-rater agreement to be reported as well, which bears most directly on claims about absolute detection performance; for a comparison between campaigns at a single site, consistency of assessment across the series is the condition that matters, and quantitative measures of contrast against local background [67] would strengthen both.

This case study represents only a single site type within its particular soil and vegetation conditions. To obtain a comprehensive understanding of the relative effectiveness of these new technologies for archaeological site assessment in the Dutch landscape (and beyond), additional test sites must be examined using comparable, standardized methodologies. In accordance with the framework articulated in the ARCfieldLAB project, these sites should be distributed as widely as possible across stratified samples of archaeological site types, soil categories, and vegetation zones, thereby enabling the development of a fully comparative database [6].

5. Conclusions

The multi-modal and multi-temporal UAV survey at 't Huis ten Bosch demonstrates both the potential and the constraints of integrating drone-based remote sensing within established archaeological prospection workflows. Across six campaigns, the combined RGB, thermal, multispectral, and elevation datasets consistently corroborated key elements of the subsurface record previously inferred from geophysics and coring, while also refining and, in some cases, extending that record in important ways. The primary moat, secondary moat and central tower and walls each exhibited distinct, recurrent features in the UAV data, consistent across sensors and campaigns with the archaeological interpretation proposed by the 2022 surveys, and clarifying aspects of their structure and infill that could not be resolved from geophysics or point-based hand-augering alone. Vice versa, some features from the latter surveys were not identified in the UAV survey.

An important conclusion therefore concerns the complementarity between techniques rather than the superiority of any one method. The moat's persistent negative cropmarks and associated thermal anomalies, linked to the rubble-rich backfill, could only be fully interpreted by drawing together coring stratigraphy, geophysical contrasts, and UAV imagery. Similarly, the robust thermal and spectral expression of the tower and wall foundations is consistent with earlier geophysical indications that demolition was incomplete and supports the inference that substantial foundation material remains in situ. Conversely, certain wall segments and finer structural details appeared either only in the geophysical data or only in specific UAV campaigns. Taken together, these patterns show that an integrated approach, combining UAV remote sensing, geophysical survey, and coring data within a single interpretative framework, yields a markedly more complete and reliable reconstruction of subsurface archaeology than any method pursued in isolation. As such, this points to

potential strategies for adoption of these techniques alongside coring in Dutch prospection practices and the AMZ-cycle.

The analysis of anomaly visibility across campaigns further highlights the crucial role of environmental and management conditions. Perhaps disappointingly, visibility did not simply track single meteorological variables, nor did it follow a uniform seasonal pattern. Instead, it appears to emerge from the interaction of soil properties, moisture history, grass phenology, mowing regime, and the timing of data acquisition. Transitional moisture and temperature conditions, rather than prolonged extremes, were repeatedly associated with the clearest thermal results, while vegetation stress related to late-season moisture deficits or specific post-mowing intervals coincided with stronger cropmarks. Comparisons with other grassland studies underscore that these relationships are strongly context-dependent: similar nominal conditions can yield different visibility outcomes under different soil and vegetation regimes, cautioning against overly generalised prescriptions for "optimal" survey timing. A distinction is worth drawing here. That the tower, the primary moat and sections of the wall foundations are repeatedly detectable, and that their visibility varies systematically between campaigns, is established by the data presented. The conditions that visibility varies with are likewise recorded in the coring record, the meteorological series, and the observed state of the vegetation at each acquisition. What this study does not establish is the physical mechanism linking the two, which would require the in situ monitoring outlined in Section 4.3.

Nevertheless, some provisional best practices can be extracted. First, the results at 't Huis ten Bosch suggest that campaigns timed around transitional rather than stable extreme conditions are particularly productive, both for thermal and spectral anomaly detection. Periods in which moderately dry spells are punctuated by one or more rainfall events, or in which the site is moving from wetter to drier states (or vice versa), appear to promote transient contrasts in soil moisture and temperature that buried features can exploit, whereas prolonged severe drought may actually suppress differential responses. This rests on six campaigns at a single site, with no direct measurement of the subsurface processes involved, and is offered as a working hypothesis for other grassland sites to test in future research. Second, survey timing should be aligned carefully with vegetation phenology and mowing. Flights very early in the growing season, when biomass is still low and the sward is uniformly vigorous, tended to yield weak spectral contrasts, while campaigns either some weeks after mowing or at the natural end of the growth cycle under moisture stress produced much stronger vegetation marks. This indicates that mowing can be used strategically but is not a prerequisite for good visibility. It is rather the interaction between cutting, regrowth, and plant water status that appears to be what matters. Third, thermal acquisitions should be scheduled preferentially for evening or night-time, when diurnal heating has peaked, and cooling is underway, and when vegetation cover is either reduced or partially stressed. Under dense, actively growing grass, the moisture contained in the sward itself, as well as evapotranspiration, dampens surface temperature contrasts, whereas sparser or stressed vegetation allows subsurface differences in thermal properties to express more clearly in the imagery. In conclusion, survey timing benefits from careful assessment based on the site-specific variables and is accordingly adapted based on temporal developments that can cause transitional events.

At the same time, the study's limitations point toward clear avenues for refinement. The restricted number of campaigns, incomplete sensor coverage, reliance on regional rather than site-specific meteorological data, and the inherently site-specific character of the results all constrain the generalisability of the patterns identified here. Addressing these limitations, through denser multi-sensor time series, local weather and soil monitoring, and

experimental expansion into UAV hyperspectral imaging, will be essential to moving from case-specific insights toward more robust comparative frameworks.

Within this broader trajectory, 't Huis ten Bosch should be viewed as a first, detailed test case, not a definitive model. Its value lies in demonstrating how multi-temporal UAV data, carefully contextualised in relation to geophysics, coring, and environmental conditions, can improve archaeological site assessment in Dutch grassland contexts. Extending this integrative, sensor-rich approach to a stratified set of sites across different soil types, hydrological regimes, and vegetation covers, along the lines proposed in ARCfieldLAB, will be necessary to establish a comparative empirical basis for evaluating the efficacy, limitations, and best-practice deployment of UAV-based prospection in the Netherlands and beyond.

Supplementary Materials: The following supporting information can be downloaded at: https://www.mdpi.com/article/10.3390/rs18213844/s1, Table S1: Flight and data capture metadata form (.xlsx), Table S2: Processing metadata form (.xlsx), Table S3: Mapped anomaly metadata form (.xlsx).

Author Contributions: Conceptualization, M.S. and J.W.; methodology, M.S. and J.W.; software, M.S. and J.W.; validation, M.S. and J.W.; formal analysis, M.S. and J.W.; data curation, M.S. and J.W.; writing—original draft preparation, M.S. and J.W.; writing—review and editing, M.S. and J.W.; visualization, M.S. and J.W.; supervision, J.W.; project administration, M.S. and J.W.; funding acquisition, J.W. All authors have read and agreed to the published version of the manuscript.

Funding: This research was supported by Bureau Monumenten en Archeologie of the Municipality of Amsterdam and the European Research Infrastructure Heritage Science (E-RIHS).

Data Availability Statement: The raw UAV data, meteorological data and the generated GIS data (including digital elevation models, thermal, and multispectral orthomosaics, derived vegetation index rasters, and anomaly mapping) will be deposited in a Zenodo repository: https://zenodo.org/communities/4drl/ https://doi.org/10.5281/zenodo.24011554 (accessed on 22 October 2026). Data are available from the corresponding author upon reasonable request in the interim.

Acknowledgments: The Huis ten Bosch case study was possible due to the initiative of Ranjith Jayasena of Bureau Monumenten en Archeologie of the Municipality of Amsterdam; we wish to thank him for the always pleasant collaboration and inspiring discussions. We wish to acknowledge Ferry van den Oever from Saricon B.V., and the colleagues at Hollandia Archeologen for their contributions to the fieldwork and research on the site in 2022, Nancy de Jong-Lambregts for her contribution to the interpretation of the results of the 2022 prospection, and Floris-Jan Bruggink for his additional observations on the recorded anomalies in his 2025 study for his virtual reconstruction of the site. We extend our gratitude to Hans Beukeboom, owner of the current Huis ten Bosch farm and adjoining fields, who has generously shared his knowledge and hospitality throughout the years. Finally, we are indebted to all who participated in the fieldwork: Mikko Kriek, Tijm Lanjouw, Markus Stoffer and Floris-Jan Bruggink.

Conflicts of Interest: The authors declare no conflicts of interest.

Abbreviations

The following abbreviations are used in this manuscript:

AMZ-cycle	Archeologische Monumentenzorg-cyclus (Archaeological Monument Care cycle)
DEM	Digital Elevation Model
DLS	Downwelling Light Sensor
DSM	Digital Surface Model
DTM	Digital Terrain Model
DTR	Diurnal Temperature Range
EVI	Enhanced Vegetation Index
GCP	Ground Control Point
GNDVI	Green Normalized Difference Vegetation Index
GNSS	Global Navigation Satellite System

IMU	Inertial Measurement Unit
KNA	Kwaliteitsnorm Nederlandse Archeologie
KNMI	Koninklijk Nederlands Meteorologisch Instituut (Royal Netherlands Meteorological Institute)
LiDAR	Light Detection and Ranging
MSAVI2	Second Modified Soil Adjusted Vegetation Index
NDRE	Normalized Difference Red Edge Index
NDVI	Normalized Difference Vegetation Index
NIR	Near-Infrared
NTRIP	Networked Transport of RTCM via Internet Protocol
PTD	Progressive TIN Densification
RTK	Real-Time Kinematic
TIN	Triangulated Irregular Network
UAV	Unmanned Aerial Vehicle

Appendix A

Table A1. The metadata schema used for the GIS-based digitisation and interpretation of anomalies across all survey datasets in this study.

Item	Description	Values	Comments
Id	Anomaly number	1-x	Simple enumerator
Rec_moment	Recording moment	e.g., 'winter', 'February, or a more specific date	Used to organize GIS layers
Sensor_vi	Sensor Visualisation	e.g., 'opt_ortho' (optical sensor, orthophoto visualization) or 'multi_ndvi' (multispectral sensor, NDVI visualization)	The sensor and the specific data model used for the mapping of anomalies
Source_lay	Source Layer	e.g., 'dem_1cmres' (LiDAR DEM data with a 1cm resolution) or 'autumn_120m_corrected_with_LP_30m' (Thermal mosaic recorded at 120m with a Low Pass filter using a 30m radius)	The specific visualization of the data used for the mapping of anomalies
Anoma_int	Interpretation of anomaly source	e.g., 'ditch outline', 'rectangular elevation', 'subsoil stone feature'	Initial mapping of all features that are not explained or not directly explained by natural or modern anthropomorphic activity
An_confid	Confidence of anomaly interpretation	0–3	'0' none (anomaly type is unknown), '1' low (anomaly interpretation is questionable), '2' medium (anomaly is clearly visible, and there are analogies to the confirmed interpretation in the area, but the morphology is not distinct), '3' high (anomaly clearly visible and has a distinct form (adapted from Lozić & Štular [65])
Visibility	How well is the anomaly visible	1–2	Referring to the local contrast that led to identification of the anomaly; '1' is poor and '2' is good (adapted from Lozić & Štular [65])
Veget_dens	How dense is the vegetation locally	1–3	Referring to local vegetation density that may obscure full identification of the anomaly; '1' negligible, '2' medium (introduces occasional and/or moderate noise) or '3' high (introduces constant and/or significant noise) (adapted from Lozić & Štular [65])

Table A1. *Cont*.

Item	Description	Values	Comments
Author	Author	e.g., 'JW' (Jitte Waagen)	The person who performs the anomaly and interpretative mapping
Date	Date	e.g., '12-04-2023'	Date of the anomaly and interpretative mapping
Arch_int	Archaeological interpretation of anomaly	e.g., 'moat outline', 'structure boundary', 'stone debris of collapsed wall'	Interpretation of anomaly in terms of the most probable archaeological explanation
Arch_confi	Confidence of archaeology interpretation	0–3	'0' none (interpretation is very uncertain), '1' low (interpretation is questionable), '2' medium (interpretation is plausible, and there are analogies to the confirmed interpretation in the area, but the morphology is not distinct), '3' high (interpretation is quite certain and has a distinct form (adapted from Lozić & Štular [65])

Appendix B

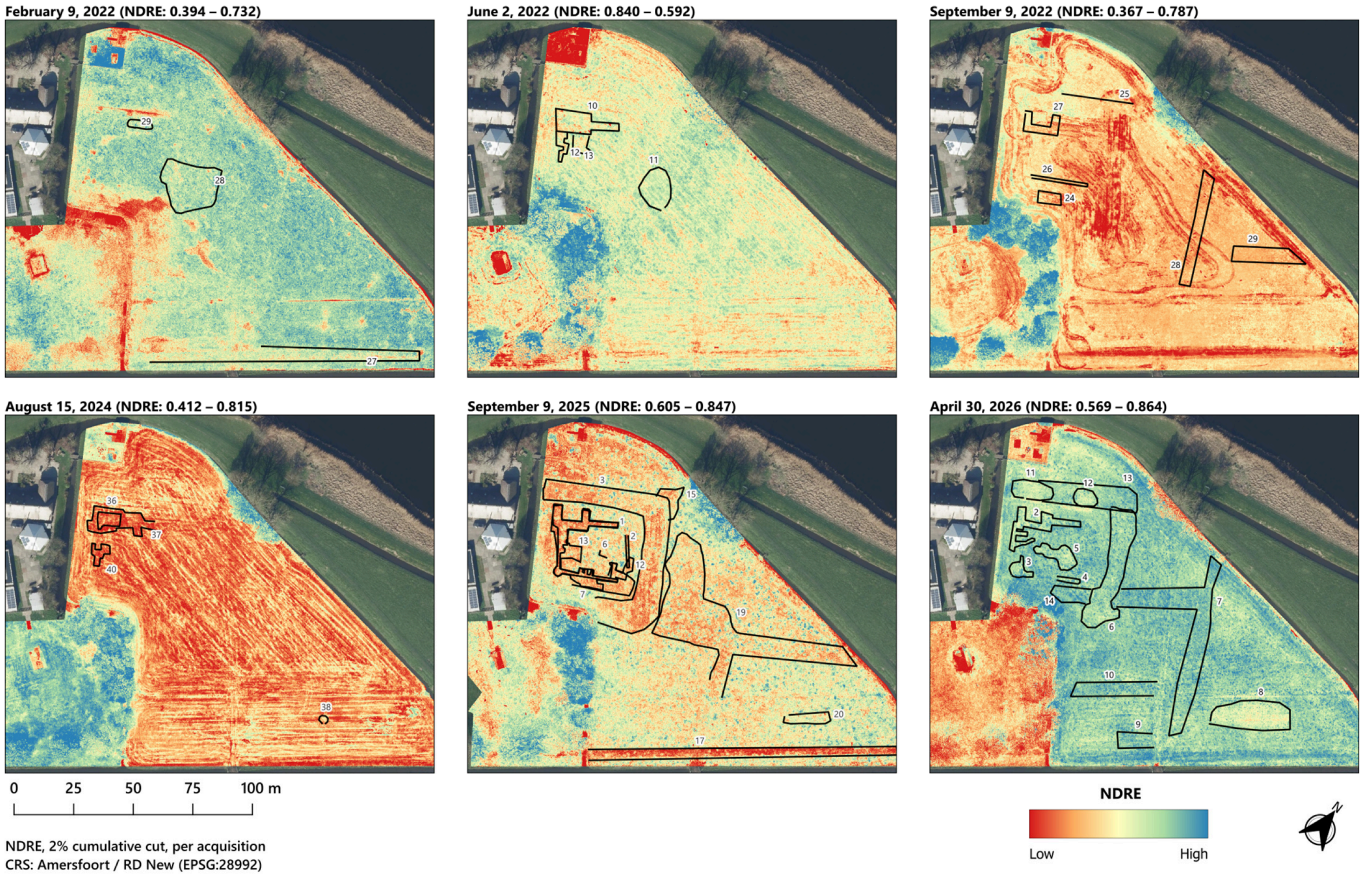


Figure A1. NDRE maps of the site 't Huis ten Bosch, Weesp, across the six UAV survey campaigns: 9 February 2022, 2 June 2022, 9 September 2022, 15 August 2024, 9 September 2025, and 30 April 2026. The digitised anomalies are shown in black. The displayed value range is given above each panel.

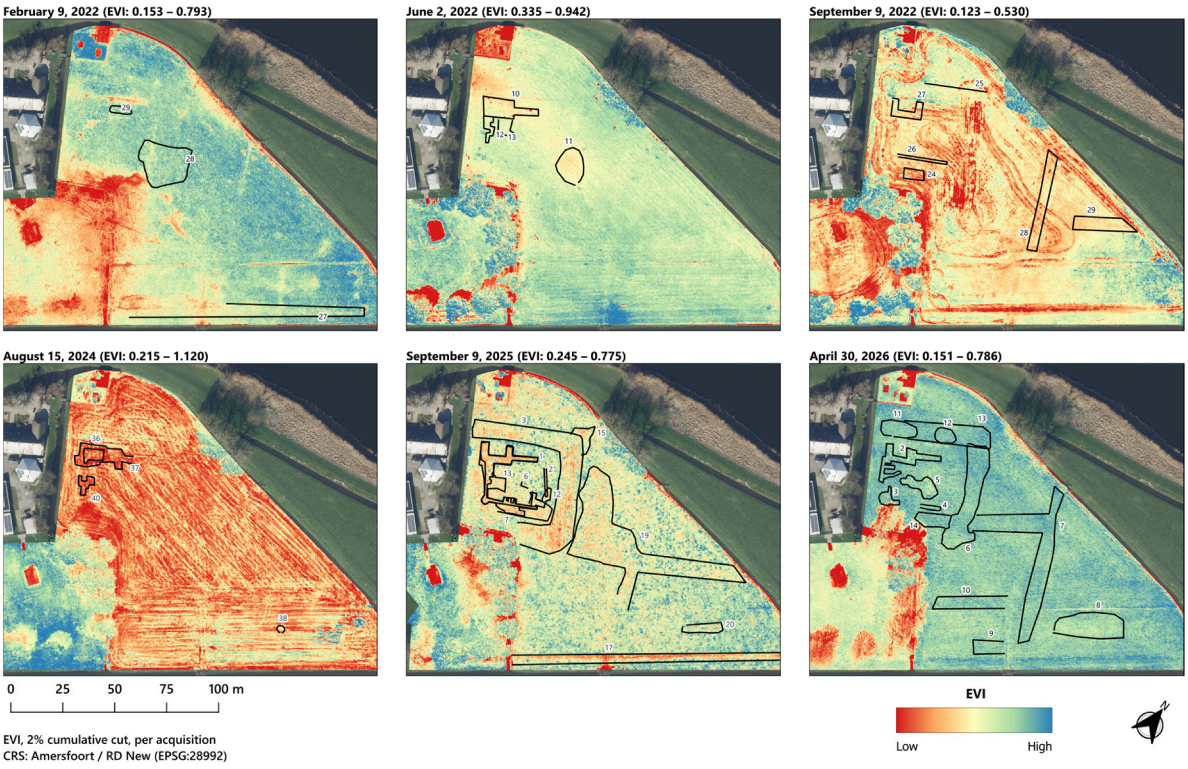


Figure A2. EVI maps of the site 't Huis ten Bosch, Weesp, across the six UAV survey campaigns: 9 February 2022, 2 June 2022, 9 September 2022, 15 August 2024, 9 September 2025, and 30 April 2026. The digitised anomalies are shown in black. The displayed value range is given above each panel.

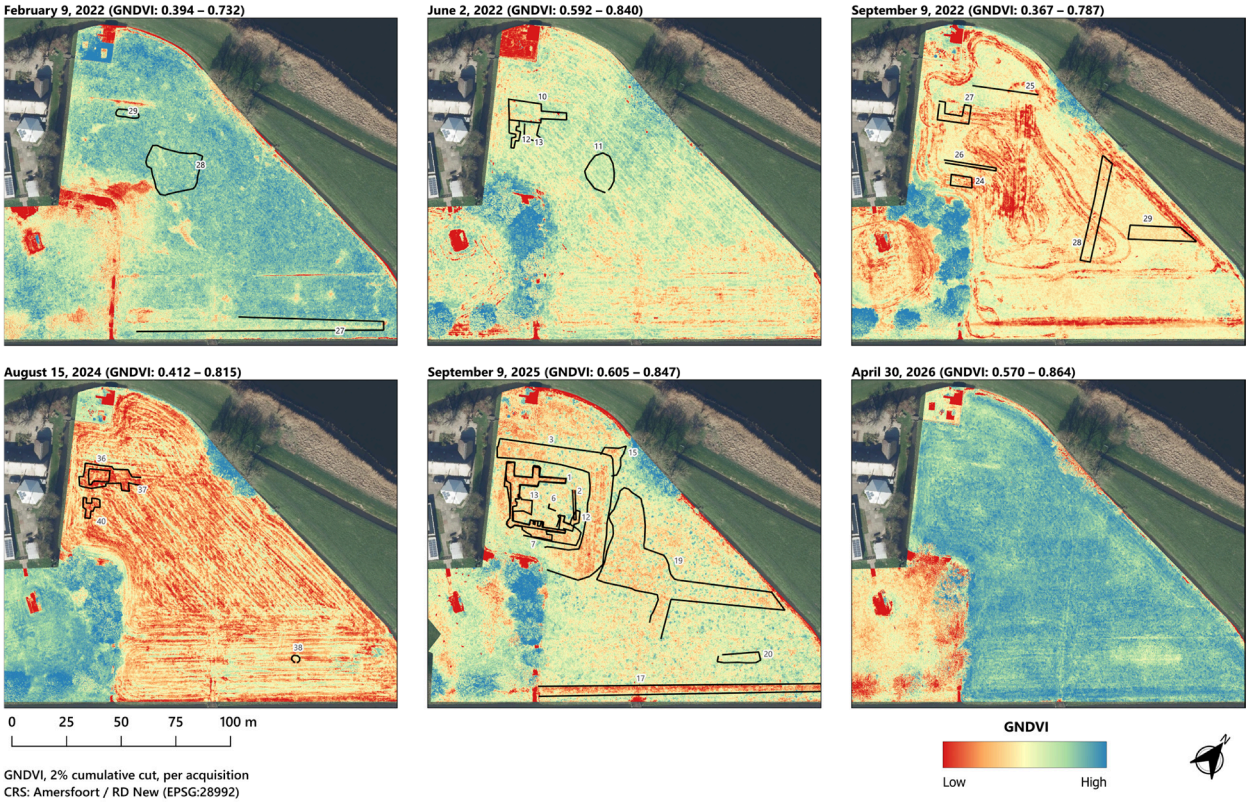


Figure A3. GNDVI maps of the site 't Huis ten Bosch, Weesp, across the six UAV survey campaigns: 9 February 2022, 2 June 2022, 9 September 2022, 15 August 2024, 9 September 2025, and 30 April 2026. The digitised anomalies are shown in black. The displayed value range is given above each panel.

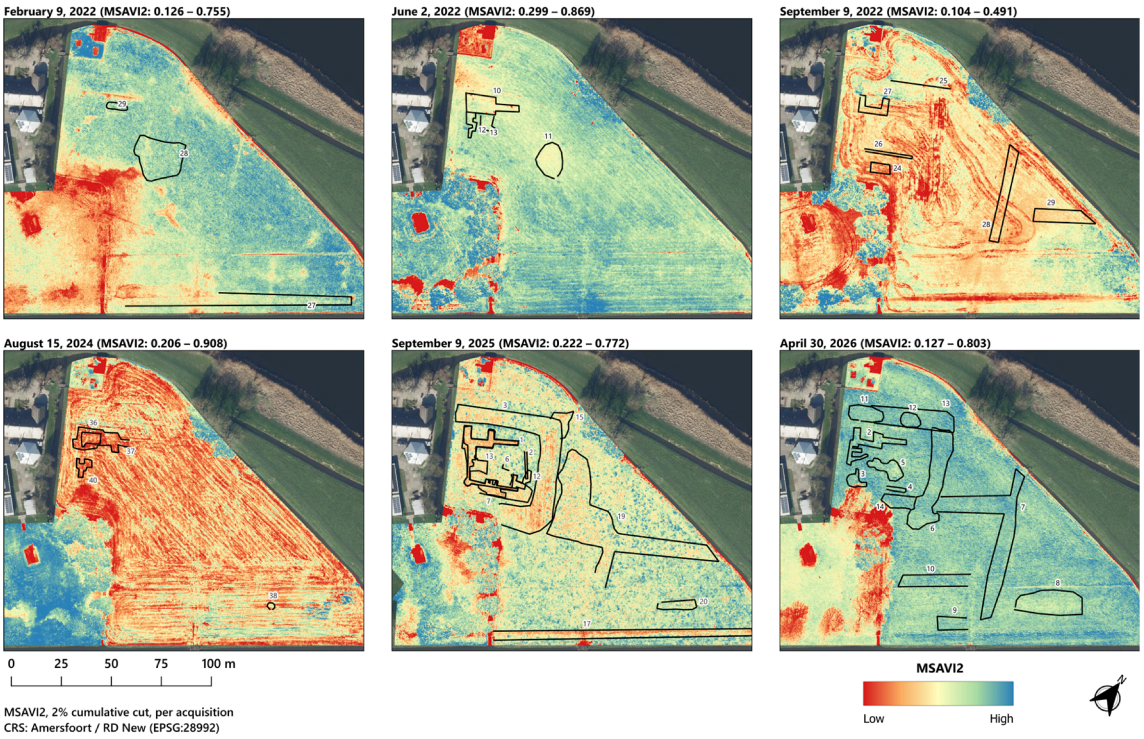


Figure A4. MSAVI2 maps of the site 't Huis ten Bosch, Weesp, across the six UAV survey campaigns: 9 February 2022, 2 June 2022, 9 September 2022, 15 August 2024, 9 September 2025, and 30 April 2026. The digitised anomalies are shown in black. The displayed value range is given above each panel.

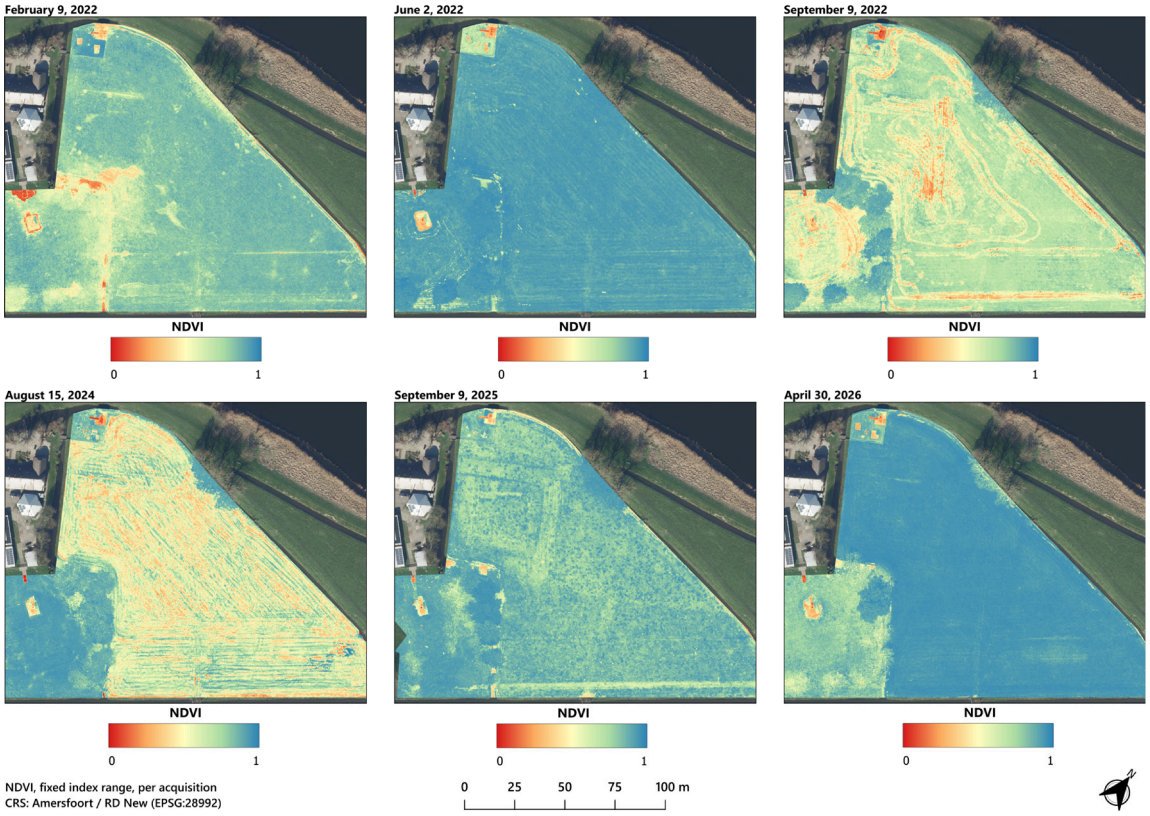


Figure A5. NDVI maps of the site 't Huis ten Bosch, Weesp, across the six UAV survey campaigns: 9 February 2022, 2 June 2022, 9 September 2022, 15 August 2024, 9 September 2025, and 30 April 2026. The display ranges are fixed between 0 and 1.

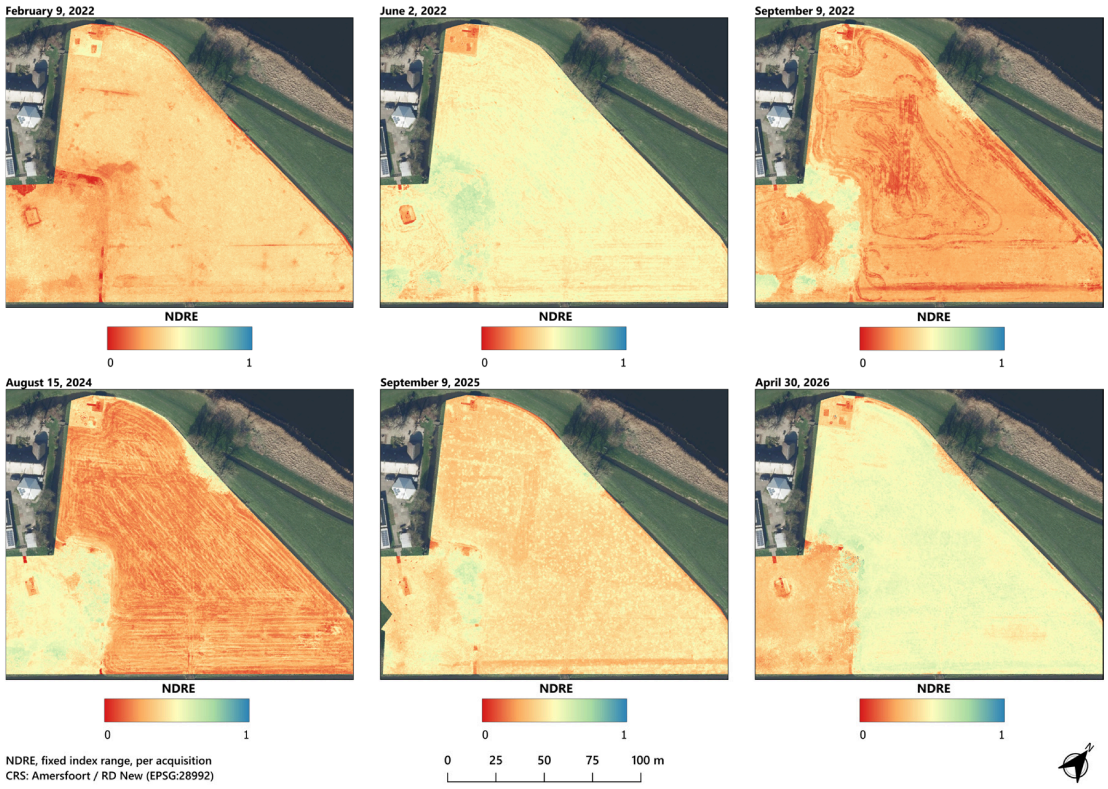


Figure A6. NDRE maps of the site 't Huis ten Bosch, Weesp, across the six UAV survey campaigns: 9 February 2022, 2 June 2022, 9 September 2022, 15 August 2024, 9 September 2025, and 30 April 2026. The display ranges are fixed between 0 and 1.

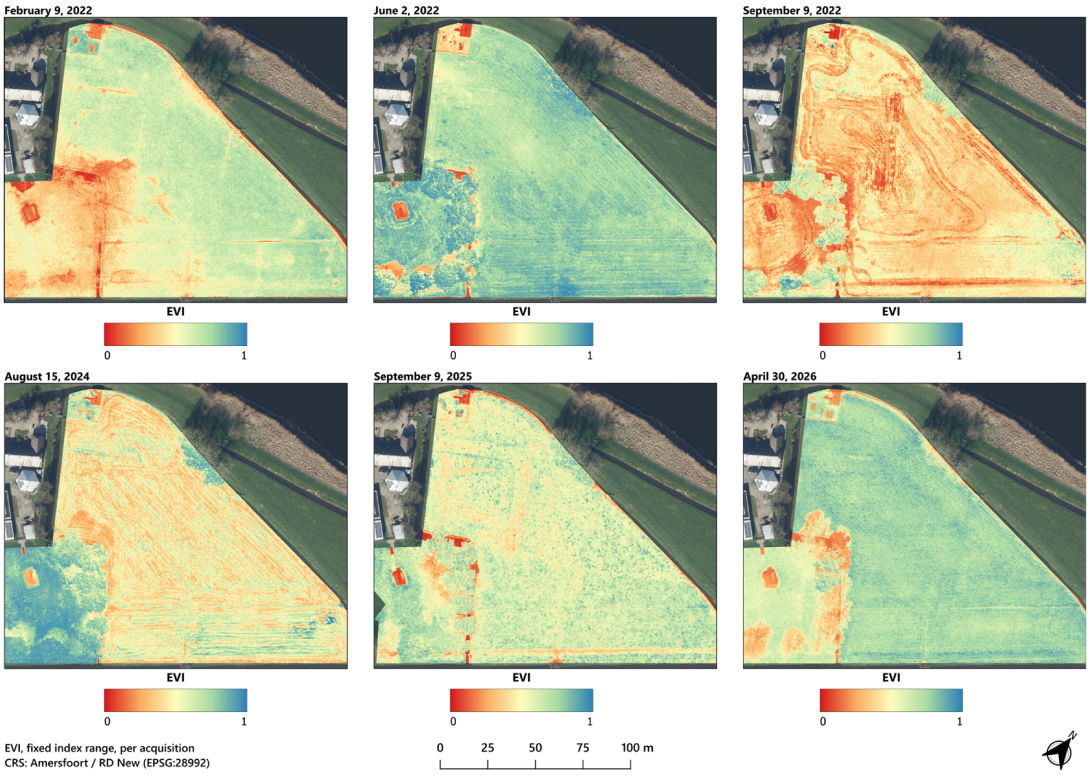


Figure A7. EVI maps of the site 't Huis ten Bosch, Weesp, across the six UAV survey campaigns: 9 February 2022, 2 June 2022, 9 September 2022, 15 August 2024, 9 September 2025, and 30 April 2026. The display ranges are fixed between 0 and 1.

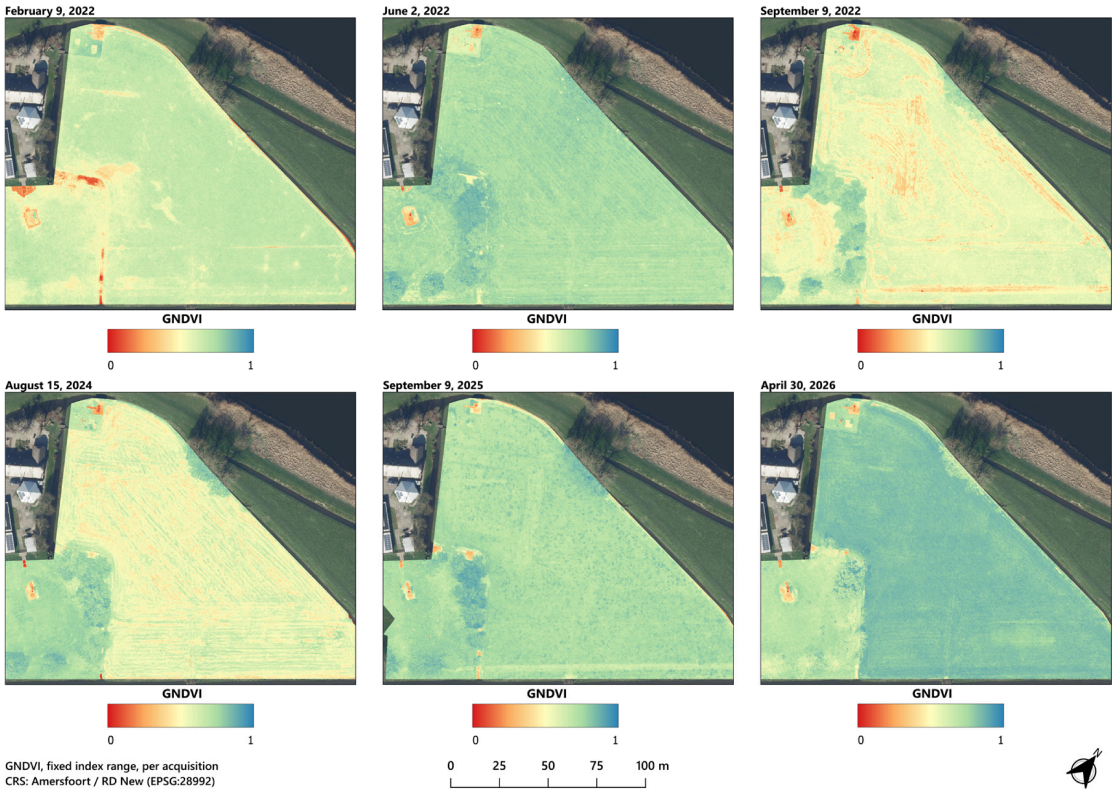


Figure A8. GNDVI maps of the site 't Huis ten Bosch, Weesp, across the six UAV survey campaigns: 9 February 2022, 2 June 2022, 9 September 2022, 15 August 2024, 9 September 2025, and 30 April 2026. The display ranges are fixed between 0 and 1.

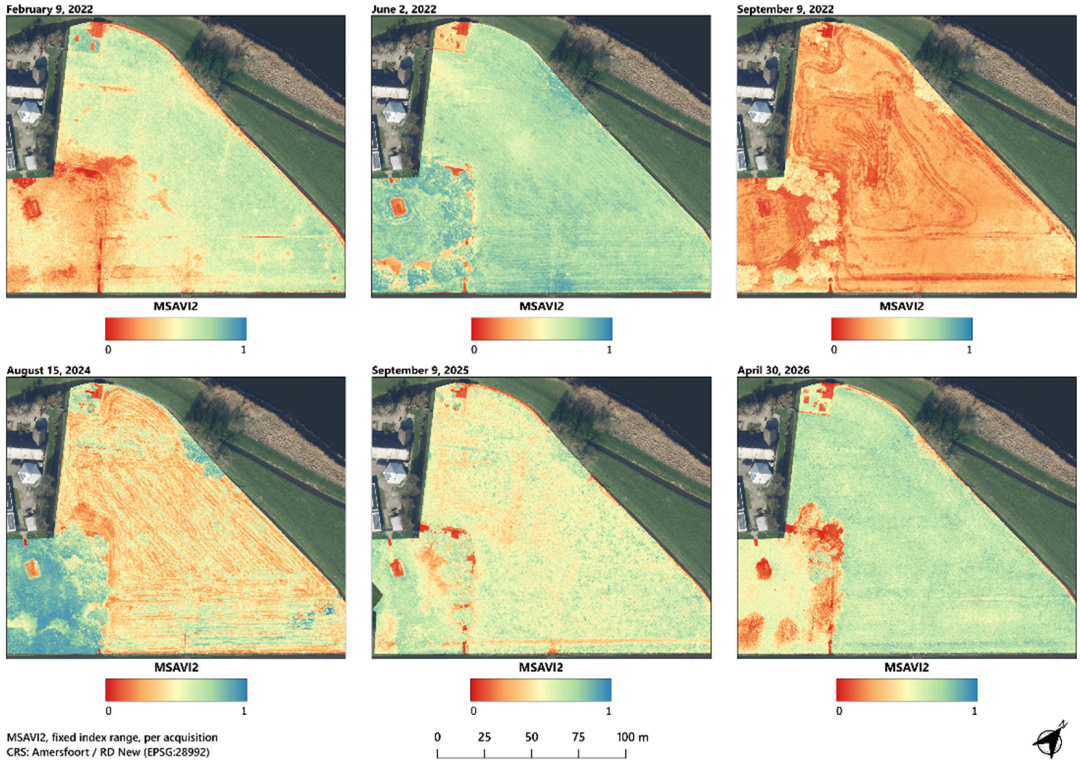


Figure A9. MSAVI2 maps of the site 't Huis ten Bosch, Weesp, across the six UAV survey campaigns: 9 February 2022, 2 June 2022, 9 September 2022, 15 August 2024, 9 September 2025, and 30 April 2026. The display ranges are fixed between 0 and 1.

References

1. Rensink, E.; de Kort, J.W.; van Doesburg, J.; Theunissen, E.M.; Bouwmeester, H.M.P. Prospection Made-to-Measure. A Digital Information System for Archaeological Prospection Methods. In *Knowledge for Informed Choices: Tools for More Effective and Efficient Selection of Valuable Archaeology in the Netherlands*; Nederlandse Archeologische Rapporten; Cultural Heritage Agency of the Netherlands (Rijksdienst voor het Cultureel Erfgoed): Amersfoort, The Netherlands, 2017; pp. 165–178.
2. Centraal College van Deskundigen (CCvD) Archeologie. *BRL SIKB 4000: Beoordelingsrichtlijn Archeologie*; Stichting Infrastructuur Kwaliteitsborging Bodembeheer: Gouda, The Netherlands, 2022.
3. Rensink, E. Geofysisch onderzoek en archeologische monumentenzorg in Nederland. In *De Toepassing van Geofysische Prospectie Methoden in de Archeologie*; Meylemans, E., De Smedt, P., Eds.; Onderzoeksrapporten Agentschap Onroerend Erfgoed; Flanders Heritage Agency (Agentschap Onroerend Erfgoed): Brussels, Belgium, 2019; pp. 35–38.
4. Rinnooy Kan, A.; Hijmans van den Bergh, C.; Raemaekers, D.; Schindler, E.; van der Steen, M. *Archeologie bij de Tijd: Aanbevelingen voor Aanpassingen*; Raad voor Cultuur: The Hague, The Netherlands, 2022.
5. Jelsma, J.; van den Oever, F.; Orbons, J.; Verschoof-van Der Vaart, W. *Meten of Vergeten: Een Inhoudelijke Evaluatie van de Toepassing van Geofysisch Onderzoek Tijdens Archeologische Prospectie van Landbodems*; Rapportage Archeologische Monumentenzorg; Cultural Heritage Agency of the Netherlands (Rijksdienst voor het Cultureel Erfgoed): Amersfoort, The Netherlands, 2021.
6. Waagen, J.; Scholte, M.; Verhagen, P.; Verschoof-van Der Vaart, W.; Visser, R.; Rensink, E. ARCfieldLAB: Stimulating Networks, Knowledge Exchange, and Experimentation in Applied Sensor Archaeology for Dutch Field Research. *Adv. Archaeol. Pract.* **2025**, *13*, 599–612. [CrossRef]
7. Campana, S. Drones in Archaeology. State-of-the-art and Future Perspectives. *Archaeol. Prospect.* **2017**, *24*, 275–296. [CrossRef]
8. Adamopoulos, E.; Rinaudo, F. UAS-Based Archaeological Remote Sensing: Review, Meta-Analysis and State-of-the-Art. *Drones* **2020**, *4*, 46. [CrossRef]
9. Waagen, J.; Sánchez, J.G.; van der Heiden, M.; Kuiters, A.; Lulof, P. In the Heat of the Night: Comparative Assessment of Drone Thermography at the Archaeological Sites of Acquarossa, Italy, and Siegerswoude, The Netherlands. *Drones* **2022**, *6*, 165. [CrossRef]
10. Bewley, R.H. Aerial Survey for Archaeology. *Photogramm. Rec.* **2003**, *18*, 273–292. [CrossRef]
11. Cowley, D.C.; Moriarty, C.; Geddes, G.; Brown, G.L.; Wade, T.; Nichol, C.J. UAVs in Context: Archaeological Airborne Recording in a National Body of Survey and Record. *Drones* **2018**, *2*, 2. [CrossRef]
12. Cuenca-García, C.; Risbøl, O.; Bates, C.R.; Stamnes, A.A.; Skoglund, F.; Ødegård, Ø.; Viberg, A.; Koivisto, S.; Fuglsang, M.; Gabler, M.; et al. Sensing Archaeology in the North: The Use of Non-Destructive Geophysical and Remote Sensing Methods in Archaeology in Scandinavian and North Atlantic Territories. *Remote Sens.* **2020**, *12*, 3102. [CrossRef]
13. Waagen, J.; Van Hilst, A. Drones over Excavations—Enhancing the Archaeologist's Eyes. An Empirical Case Study into the Deployment of UAS Remote Sensing as a Research Tool for Archaeological Excavation, in Veldhoven, the Netherlands. *J. Archaeol. Sci. Rep.* **2025**, *62*, 105043. [CrossRef]
14. Rensink, E.; Theunissen, L.; Feiken, H.; Bourgeois, J.; Deforce, K.; van Doesburg, J.; Emaus, R.; Van Der Heiden, M.; de Jong-Lambregts, N.; Karagiannis, N.; et al. *Vanuit de Lucht Zie Je Meer: Remote Sensing in de Nederlandse Archeologie*; Nederlandse Archeologische Rapporten; Cultural Heritage Agency of the Netherlands (Rijksdienst voor het Cultureel Erfgoed): Amersfoort, The Netherlands, 2022.
15. Emaus, R. Cutting Through the Green: A Case for Grassland Archaeology Using UAV Multispectral Data. *Archaeol. Prospect.* **2026**, *33*, 327–337. [CrossRef]
16. Trachet, J.; Bäumler, S.; Krojer, S.; Verhegge, J.; De Clercq, W.; De Smedt, P.; Maes, W.H.; Majchczack, B.S.; Trinks, I.; Wilken, D. Optimizing Strategies for Non-Invasive Prospection of Settlements in the Intertidal Zone: A Case Study from the Centre of the Drowned Medieval Village of Tolsende (Scheldt Estuary, the Netherlands). *Archaeol. Prospect.* **2026**, 1–11. [CrossRef]
17. Kozioł, K.; Borowiec, N.; Marmol, U.; Rzeszutek, M.; Santos, C.A.G.; Czerniec, J. Machine Learning-Based Detection of Archeological Sites Using Satellite and Meteorological Data: A Case Study of Funnel Beaker Culture Tombs in Poland. *Remote Sens.* **2025**, *17*, 2225. [CrossRef]
18. Verhoeven, G.J. Near-Infrared Aerial Crop Mark Archaeology: From Its Historical Use to Current Digital Implementations. *J. Archaeol. Method Theory* **2012**, *19*, 132–160. [CrossRef]
19. Stanjek, H.; Faßbinder, J.W.E. Soil Aspects Affecting Archaeological Details in Aerial Photographs. *Archaeol. Prospect.* **1995**, *2*, 91–101. [CrossRef]
20. Casana, J.; Wiewel, A.; Cool, A.; Hill, A.C.; Fisher, K.D.; Laugier, E.J. Archaeological Aerial Thermography in Theory and Practice. *Adv. Archaeol. Pract.* **2017**, *5*, 310–327. [CrossRef]
21. Casana, J.; Fowles, S.; Montgomery, L.M.; Mermejo, R.; Ferwerda, C.; Hill, A.C.; Adler, M. Multi-Sensor Drone Survey of Ancestral Agricultural Landscapes at Picuris Pueblo, New Mexico. *J. Archaeol. Sci.* **2023**, *157*, 105837. [CrossRef]

22. Salgado Carmona, J.Á.; Quirós, E.; Mayoral, V.; Charro, C. Assessing the Potential of Multispectral and Thermal UAV Imagery from Archaeological Sites. A Case Study from the Iron Age Hillfort of Villasviejas Del Tamuja (Cáceres, Spain). *J. Archaeol. Sci. Rep*. **2020**, *31*, 102312. [CrossRef]
23. James, K.; Nichol, C.J.; Wade, T.; Cowley, D.; Gibson Poole, S.; Gray, A.; Gillespie, J. Thermal and Multispectral Remote Sensing for the Detection and Analysis of Archaeologically Induced Crop Stress at a UK Site. *Drones* **2020**, *4*, 61. [CrossRef]
24. Hill, A.C.; Laugier, E.J.; Casana, J. Archaeological Remote Sensing Using Multi-Temporal, Drone-Acquired Thermal and Near Infrared (NIR) Imagery: A Case Study at the Enfield Shaker Village, New Hampshire. *Remote Sens*. **2020**, *12*, 690. [CrossRef]
25. Ronchi, D.; Limongiello, M.; Demetrescu, E.; Ferdani, D. Multispectral UAV Data and GPR Survey for Archeological Anomaly Detection Supporting 3D Reconstruction. *Sensors* **2023**, *23*, 2769. [CrossRef]
26. McLeester, M.; Casana, J.; Schurr, M.R.; Hill, A.C.; Wheeler, J.H. Detecting Prehistoric Landscape Features Using Thermal, Multispectral, and Historical Imagery Analysis at Midewin National Tallgrass Prairie, Illinois. *J. Archaeol. Sci. Rep*. **2018**, *21*, 450–459. [CrossRef]
27. Brooke, C.; Clutterbuck, B. Mapping Heterogeneous Buried Archaeological Features Using Multisensor Data from Unmanned Aerial Vehicles. *Remote Sens*. **2020**, *12*, 41. [CrossRef]
28. Jayasena, R.M.; de Jong-Lambregts, N.; van den Oever, F.; Waagen, J. Het Verdwenen Kasteel van Weesp: Een Archeologische Verkenning Naar Het Dertiende-Eeuwse Huis Ten Bosch. *Amstelodamum* **2023**, *3*, 133–137.
29. Jayasena, R.M. Power Games and Conspiracies Reflected in Amsterdam's 13th-Century Urban Development. In *Lübecker Kolloquium zur Stadtarchäologie im Hanseraum XII: Adel in der Stadt. Archäologie im Kontext Mittelalterlicher Urbaner Eliten*; Rieger, D., Ed.; LübeckVerlag Marie Leidorf GmbH: Lübeck, Germany, 2024; pp. 119–133.
30. Groesbeek, J.W. *Middeleeuwse Kastelen van Noord-Holland: Hun Bewoners En Bewogen Geschiedenis*; Elmar: Amersfoort, The Netherlands, 1981.
31. van den Oever, F.; de Jong-Lambregts, N. *Gecombineerd Geofysisch Onderzoek Huis ten Bosch te Weesp (Gemeente Amsterdam)*; Saricon B.V.: Sliedrecht, The Netherlands, 2023.
32. Dautzenberg, M.J.J.; Floore, P.M. *Huis ten Bosch, Uitermeer, Weesp, een Karterend Booronderzoek*; Hollandia Reeks; Hollandia Archeologen: Zaandijk, The Netherlands, 2022.
33. Czajlik, Z.; Árvai, M.; Mészáros, J.; Nagy, B.; Rupnik, L.; Pásztor, L. Cropmarks in Aerial Archaeology: New Lessons from an Old Story. *Remote Sens*. **2021**, *13*, 1126. [CrossRef]
34. MicaSense RedEdge-MX Integration Guide. Available online: https://support.micasense.com/hc/en-us/articles/360011389334-RedEdge-MX-Integration-Guide (accessed on 27 July 2026).
35. MicaSense RedEdge-P Integration Guide. Available online: https://support.micasense.com/hc/en-us/articles/4410824602903-RedEdge-P-Integration-Guide (accessed on 27 July 2026).
36. DJI Zenmuse XT2. Available online: https://www.dji.com/nl/support/product/zenmuse-xt2 (accessed on 27 July 2026).
37. DJI Zenmuse H30 Series—Specs. Available online: https://enterprise.dji.com/zenmuse-h30-series/specs (accessed on 27 July 2026).
38. Cool, A.C. Thermography. In *The Encyclopedia of Archaeological Sciences*; López Varela, S.L., Ed.; Wiley: Hoboken, NJ, USA, 2018; pp. 1–5.
39. Kuenzer, C.; Dech, S. Theoretical Background of Thermal Infrared Remote Sensing. In *Thermal Infrared Remote Sensing: Sensors, Methods, Applications*; Remote Sensing and Digital Image Processing; Springer: Dordrecht, The Netherlands, 2013; pp. 1–26.
40. Ciccone, G. Thermal Analysis of Evapotranspiration in Cultivated Fields for the Detection of Archaeological Anomalies. *Archaeol. Prospect*. **2024**, *31*, 217–231. [CrossRef]
41. Hall, N.; Ernenwein, E.G. Optimizing UAS Thermal Imaging for Archaeological Prospection: Effects of Time of Day, Season, and Surface Conditions at a Historic African American Cemetery. *J. Archaeol. Sci*. **2026**, *188*, 106501. [CrossRef]
42. DJI Zenmuse L1. Available online: https://www.dji.com/nl/support/product/zenmuse-l1 (accessed on 27 July 2026).
43. DJI Zenmuse L2—Specs. Available online: https://enterprise.dji.com/zenmuse-l2/specs (accessed on 27 July 2026).
44. DJI Zenmuse X5S. Available online: https://www.dji.com/nl/support/product/zenmuse-x5s (accessed on 22 October 2026).
45. DJI Zenmuse P1—Specs. Available online: https://enterprise.dji.com/zenmuse-p1 (accessed on 27 July 2026).
46. Dawson, N.; Fischer, J.; Kuhn, M.; Pasotti, A.; mhugent; Rouzaud, D.; Bruy, A.; Sutton, T.; Dobias, M.; Pellerin, M.; et al. Qgis/QGIS: 3.44.8. Available online: https://zenodo.org/doi/10.5281/zenodo.18889145 (accessed on 27 July 2026).
47. Rouse, J.W.; Haas, R.H.; Schell, J.A.; Deering, D.W. Monitoring Vegetation Systems in the Great Plains with ERTS. In Proceedings of the 3rd Earth Resources Technology Satellite Symposium, Washington, DC, USA, 10–14 December 1974.
48. Barnes, E.M.; Clarke, T.R.; Richards, S.E.; Colaizzi, P.D.; Haberland, J.; Kostrzewski, M.; Waller, P.; Choi, C.; Riley, E.; Thompson, T.; et al. Coincident Detection of Crop Water Stress, Nitrogen Status and Canopy Density Using Ground Based Multispectral Data. In Proceedings of the Fifth International Conference on Precision Agriculture and Other Resource Management, Bloomington, MN, USA, 16–19 July 2000.

49. Gitelson, A.A.; Kaufman, Y.J.; Merzlyak, M.N. Use of a Green Channel in Remote Sensing of Global Vegetation from EOS-MODIS. *Remote Sens. Environ.* **1996**, *58*, 289–298. [CrossRef]
50. Qi, J.; Chehbouni, A.; Huete, A.R.; Kerr, Y.H.; Sorooshian, S. A Modified Soil Adjusted Vegetation Index. *Remote Sens. Environ.* **1994**, *48*, 119–126. [CrossRef]
51. Huete, A.; Didan, K.; Miura, T.; Rodriguez, E.P.; Gao, X.; Ferreira, L.G. Overview of the Radiometric and Biophysical Performance of the MODIS Vegetation Indices. *Remote Sens. Environ.* **2002**, *83*, 195–213. [CrossRef]
52. DJI. *DJI Thermal Analysis Tool 3 User Manual V1.8*; DJI: Shenzhen, China, 2025. Available online: https://terra-1-g.djicdn.com/2640963bcd8e45c0a4f0cb9829739d6b/20250916/DJI%20Thermal%20Analysis%20Tool%203_User%20Guide_en.pdf (accessed on 27 July 2026).
53. UAV4GEO Thermal Tools. 2025. Available online: https://github.com/uav4geo/Thermal-Tools/releases/tag/v1.2.0 (accessed on 27 July 2026).
54. Paulsen, P.; Ferwerda, C.; Lehner, J.W.; Harrower, M.J.; Zaribaf, A.; Creamer, P.; Casana, J. Drone-Based Thermal Imaging of Subsurface Architecture: Methodological Insights and Discoveries at Iron Age Raki (Oman). *J. Archaeol. Sci. Rep.* **2026**, *69*, 105569. [CrossRef]
55. Conrad, O.; Bechtel, B.; Bock, M.; Dietrich, H.; Fischer, E.; Gerlitz, L.; Wehberg, J.; Wichmann, V.; Böhner, J. System for Automated Geoscientific Analyses (SAGA) v. 2.1.4. *Geosci. Model Dev.* **2015**, *8*, 1991–2007. [CrossRef]
56. DJI. DJI Terra. Available online: https://enterprise.dji.com/dji-terra (accessed on 27 July 2026).
57. BayesMap Solutions BayesStripAlign 2.27. Available online: https://bayesmap.com/products/bayesstripalign/ (accessed on 27 July 2026).
58. rapidlasso GmbH LAStools 2.0.4. Available online: https://rapidlasso.de/product-overview/ (accessed on 27 July 2026).
59. Roussel, J.-R.; Auty, D. lidR: Airborne LiDAR Data Manipulation and Visualization for Forestry Applications (v4.3.2). Available online: https://cran.r-project.org/package=lidR (accessed on 27 July 2026).
60. Roussel, J.-R.; Auty, D.; Coops, N.C.; Tompalski, P.; Goodbody, T.R.H.; Meador, A.S.; Bourdon, J.-F.; De Boissieu, F.; Achim, A. lidR: An R Package for Analysis of Airborne Laser Scanning (ALS) Data. *Remote Sens. Environ.* **2020**, *251*, 112061. [CrossRef]
61. Axelsson, P. DEM Generation from Laser Scanner Data Using Adaptive TIN Models. *Int. Arch. Photogramm. Remote Sens.* **2000**, *33*, 110–117.
62. Pix4D SA PIX4Dmapper 4.10.1. Available online: https://www.pix4d.com/product/pix4dmapper-photogrammetry-software/ (accessed on 27 July 2026).
63. Agisoft LLC Agisoft Metashape Professional Edition (v2.3.1). Available online: https://www.agisoft.com/features/professional-edition/ (accessed on 27 July 2026).
64. Waagen, J. Documenting Drone Remote Sensing: A Reality-Based Modelling Approach for Applications in Cultural Heritage and Archaeology. *Drone Syst. Appl.* **2025**, *13*, 1–14. [CrossRef]
65. Lozić, E.; Štular, B. Documentation of Archaeology-Specific Workflow for Airborne LiDAR Data Processing. *Geosciences* **2021**, *11*, 26. [CrossRef]
66. Agapiou, A.; Hadjimitsis, D.G.; Sarris, A.; Georgopoulos, A.; Alexakis, D.D. Optimum Temporal and Spectral Window for Monitoring Crop Marks over Archaeological Remains in the Mediterranean Region. *J. Archaeol. Sci.* **2013**, *40*, 1479–1492. [CrossRef]
67. Kalayci, T.; Lasaponara, R.; Wainwright, J.; Masini, N. Multispectral Contrast of Archaeological Features: A Quantitative Evaluation. *Remote Sens.* **2019**, *11*, 913. [CrossRef]
68. Koninklijk Nederlands Meteorologisch Instituut (KNMI). Daggegevens van het weer in Nederland. Available online: https://www.knmi.nl/nederland-nu/klimatologie/daggegevens (accessed on 22 October 2026).
69. Netherlands Space Agency (NLSA). Satellietdataportaal. Available online: https://www.satellietdataportaal.nl/ (accessed on 27 July 2026).
70. Bruggink, F.J. *4DRL Report Series 15—Reconstructing 't Huijs Ten Bosch*; University of Amsterdam: Amsterdam, The Netherlands, 2026. Available online: https://uvaauas.figshare.com/articles/journal_contribution/4DRL_Report_Series_15_-_Reconstructing_t_Huijs_ten_Bosch/31672438/1/files/62695132.pdf (accessed on 22 October 2026).
71. Agapiou, A.; Hegyi, A.; Stavilă, A. Observations of Archaeological Proxies through Phenological Analysis over the Megafort of Csanádpalota-Juhász T. Tanya in Hungary Using Sentinel-2 Images. *Remote Sens.* **2023**, *15*, 464. [CrossRef]
72. Gojda, M.; Hejcman, M. Cropmarks in Main Field Crops Enable the Identification of a Wide Spectrum of Buried Features on Archaeological Sites in Central Europe. *J. Archaeol. Sci.* **2012**, *39*, 1655–1664. [CrossRef]
73. Thürkow, F.; Teucher, M.; Thürkow, D.; Mohri, M. Stone Detection on Agricultural Land Using Thermal Imagery from Unmanned Aerial Systems. *AgriEngineering* **2025**, *7*, 203. [CrossRef]
74. Bennett, R.; Welham, K.; Hill, R.A.; Ford, A. Airborne Spectral Imagery for Archaeological Prospection in Grassland Environments—An Evaluation of Performance. *Antiquity* **2013**, *87*, 220–236. [CrossRef]

75. Moriarty, C.; Cowley, D.C.; Wade, T.; Nichol, C.J. Deploying Multispectral Remote Sensing for Multi-Temporal Analysis of Archaeological Crop Stress at Ravenshall, Fife, Scotland. *Archaeol. Prospect.* **2019**, *26*, 33–46. [CrossRef]
76. Scollar, I.; Tabbagh, A.; Hesse, A.; Herzog, I. *Archaeological Prospecting and Remote Sensing*; Topics in Remote Sensing; Cambridge University Press: Cambridge, UK, 1990.
77. Materazzi, F.; Pacifici, M.; Santaga, F.S. From Top to Bottom Multispectral Remote Sensing and Data Integration to Rediscover Veii. *J. Fasti Online* **2024**, *577*.
78. Casana, J.; Ferwerda, C. Drone-Acquired Short-Wave Infrared (SWIR) Imagery in Landscape Archaeology: An Experimental Approach. *Remote Sens.* **2024**, *16*, 1671. [CrossRef]
79. Casana, J.; Ferwerda, C. Archaeological Prospection Using WorldView-3 Short-wave Infrared (SWIR) Satellite Imagery: Case Studies from the Fertile Crescent. *Archaeol. Prospect.* **2023**, *30*, 327–340. [CrossRef]

Disclaimer/Publisher's Note: The statements, opinions and data contained in all publications are solely those of the individual author(s) and contributor(s) and not of MDPI and/or the editor(s). MDPI and/or the editor(s) disclaim responsibility for any injury to people or property resulting from any ideas, methods, instructions or products referred to in the content.